PETROGENESIS AND RARE EARTH ELEMENT ECONOMIC POTENTIAL OF PILOT KNOB, A PLIOCENE (?) ALKALINE INTRUSIVE COMPLEX IN THE TOGWOTEE PASS REGION, NORTHWESTERN WYOMING (U.S.A)

by

ZACHARY CALEB DODD

B.S., Kansas State University, 2013

A THESIS

submitted in partial fulfillment of the requirements for the degree

MASTER OF SCIENCE

Department of Geology
College of Arts and Sciences

KANSAS STATE UNIVERSITY
Manhattan, Kansas

2015

Approved by:

Major Professor
Dr. Matthew Brueseke

Abstract

Previous K-Ar dating and petrography (Obradovich, 1978) have identified Pilot Knob as an ~3.4 (±0.06) Ma alkaline intrusive body. Bulk rock geochemistry obtained via XRF from four samples of Pilot Knob verifies the transitionally alkaline composition of the body, and new REE data also show enriched La, Ce, and Nd concentrations, consistent with rare earth element (REE) enrichment. Given the increased demand for REEs over the past ~30 years and China accounting for > 90% of global REE production (Kynicky, et al. 2012), it is important to evaluate new domestic REE sources. This includes those associated with alkaline intrusive complexes, because they are demonstrated to host high REE concentrations (Verplanck and Van Gosen, 2011). Such alkaline igneous occurrences show complex mineralization and consist of many minerals containing substitutional REEs (Mariano and Mariano, 2012). This study evaluates the petrogenesis and mineralogy of Pilot Knob (and a secondary field site, Wildcat Hill) and determines whether the intrusive body is consistent with an economically viable REE deposit. Additionally, given its geographic location and Pliocene faulting and magmatism (e.g., predating the earliest volcanism at Yellowstone), Pilot Knob may represent one of the earliest structural manifestations of the "arrival" of the Yellowstone hotspot at its current location under the North American lithosphere or magmatism associated with lithospheric extension to the south at the Leucite Hills, WY. Inspection of satellite imagery, which has been verified with field data, shows that other intrusive igneous bodies (e.g. - Wildcat Hill) exist, along an apparent normal fault zone along strike with a major extensionally related fault zone documented ~10 km northwest of Pilot Knob. Clinopyroxene geobarometry, coupled with Nd isotope data ($\varepsilon Nd_{3.5Ma}$ = -21.9), indicates that Pilot Knob formed via a multi-stage development history that initiated with melting of ancient lithospheric mantle, where crystallization occurred at a variety of depths. As an alkaline intrusive complex, Pilot Knob has been identified, based on mineral and chemical compositions, as a kersantite, and has been found to contain approximately 600 ppm total light-rare earth element ore lode with ~150 ppm Nd, ~175 ppm La, and ~338 ppm Ce enrichment. Apatite was found to be the primary REE-bearing mineral via petrography and electron microprobe analyses. Based on current technology and processing methods, REE concentrations were not found to be significant enough to denote an economically viable REE ore deposit at Pilot Knob.

Table of Contents

List of Figures

List of Tables

Acknowledgements

Thank you to Dr. Matthew Brueseke for his vast knowledge in petrology and general geology, as well as his immeasurable time spent discussing my thesis. Thanks also to my committee members Dr. Pamela Kempton and Dr. Matthew Kirk for their help and advice. Thank you to the Society of Economic Geologists (SEG), who made this project possible through their generous grant, Dr. John Morton at Miami University, and Dr. Jeff Vervoort at Washington State University. Also thanks to the Anna Downey for her help in the field, the Wells family for their hospitality at the Timberline Ranch in Dubois, WY during our field work, to Dr. Julien Allaz from Colorado University for his time and knowledge with the electron microprobe, and my classmates for their encouragement and suggestions. Last, but certainly not least, thanks to my wife for her constant patience, her unwavering encouragement, and her constant faith in me that I would complete this project.

Chapter 1 - INTRODUCTION

Prior K-Ar age dating and petrographic inspection (Obradovich, 1978) identified Pilot Knob as an ~3.4 (±0.06) Ma alkaline intrusive complex; this was solely on the basis of petrography. Additional bulk rock geochemistry from one sample in 2013 indicated elevated LREE occurrence possibly indicative of an economic source. The purpose of this study is to [1] decipher the origin of Pilot Knob (and secondarily, Wildcat Hill, an intrusive body ~12 km to the northwest along a postulated normal fault zone) via a study involving geological mapping and sampling, petrography, bulk rock major and trace element chemistry, mineral chemistry, and radiogenic isotope constraints; and [2] to evaluate whether Pilot Knob is characterized by REE enrichments consistent with an economically viable ore deposit.

1.1 Study Area

The Togwotee Pass region in northwest Wyoming, U.S.A., is located near the western portion of the Upper Wind River Basin (UWRB) and is a structurally complicated and geologically complex region, which includes young, <5 Ma igneous activity (Figure 1-1). Although a substantial amount of literature exists covering the sedimentary rocks and Absoraka volcanics in the region, very little information currently exists on the development or composition of young (<5 Ma) igneous complexes that appear to be present throughout the region. As a further complication, accessibility is limited in much of the region due to the remoteness of the locations. Further study is required to better understand the geologic constraints on the regional young igneous complexes and their relationships with the surrounding sedimentary and volcaniclastic strata. The study area of this project (Figure 1-1) is located directly over the continental divide in Togwotee Pass and is comprised of two intrusions (Figure 1-2), Pilot Knob and previously unnamed Wildcat Hill, with an emphasis on Pilot Knob.

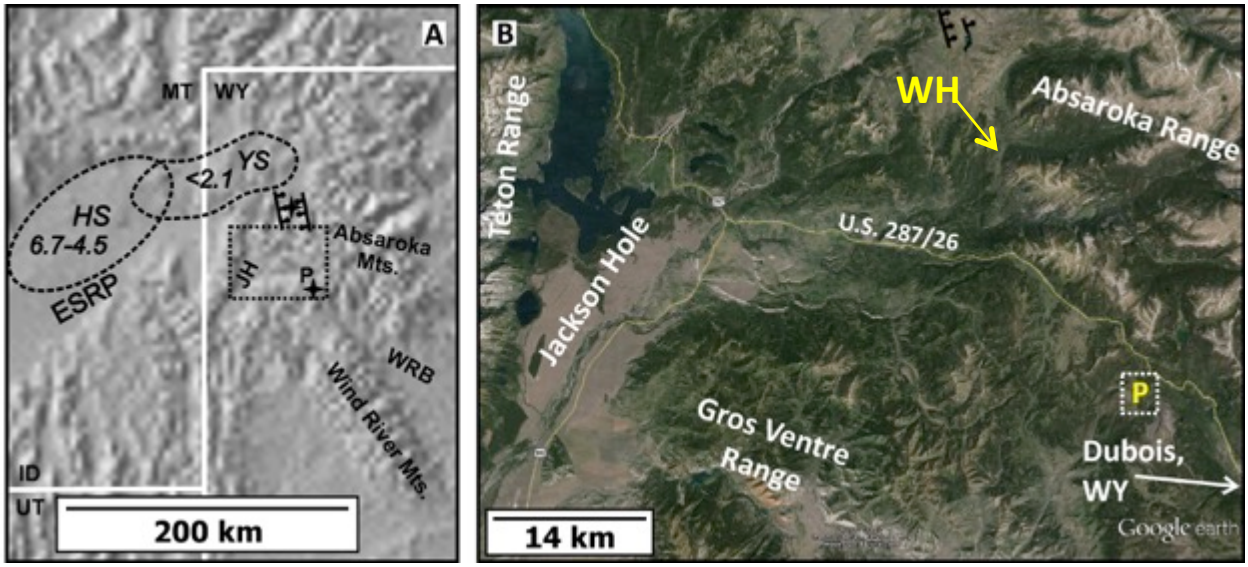

Figure 1-1 – Study area, Togwotee Pass Region, WY

(A) Digital elevation model showing the location of Snake River Plain-Yellowstone volcanic fields (dashed ovals), extra-caldera basalt occurrences south of the active Yellowstone volcanic field (black stars), and study area (black dashed box). H, Heise; Y, Yellowstone; numbers are ages, Ma, when the volcanic fields were active. JH, Jackson Hole, WY; WRB, Wind River basin. Black hachured lines are northwest-southeast trending extensional fault zone that extends from Yellowstone

(B) Google Earth satellite image showing study area (black dashed box in Figure 1-1A). P, Pilot Knob; WH, Wildcat Hill; hachured lines are northwest-southeast trending extensional fault zones. Dashed white box is Pilot Knob field area.

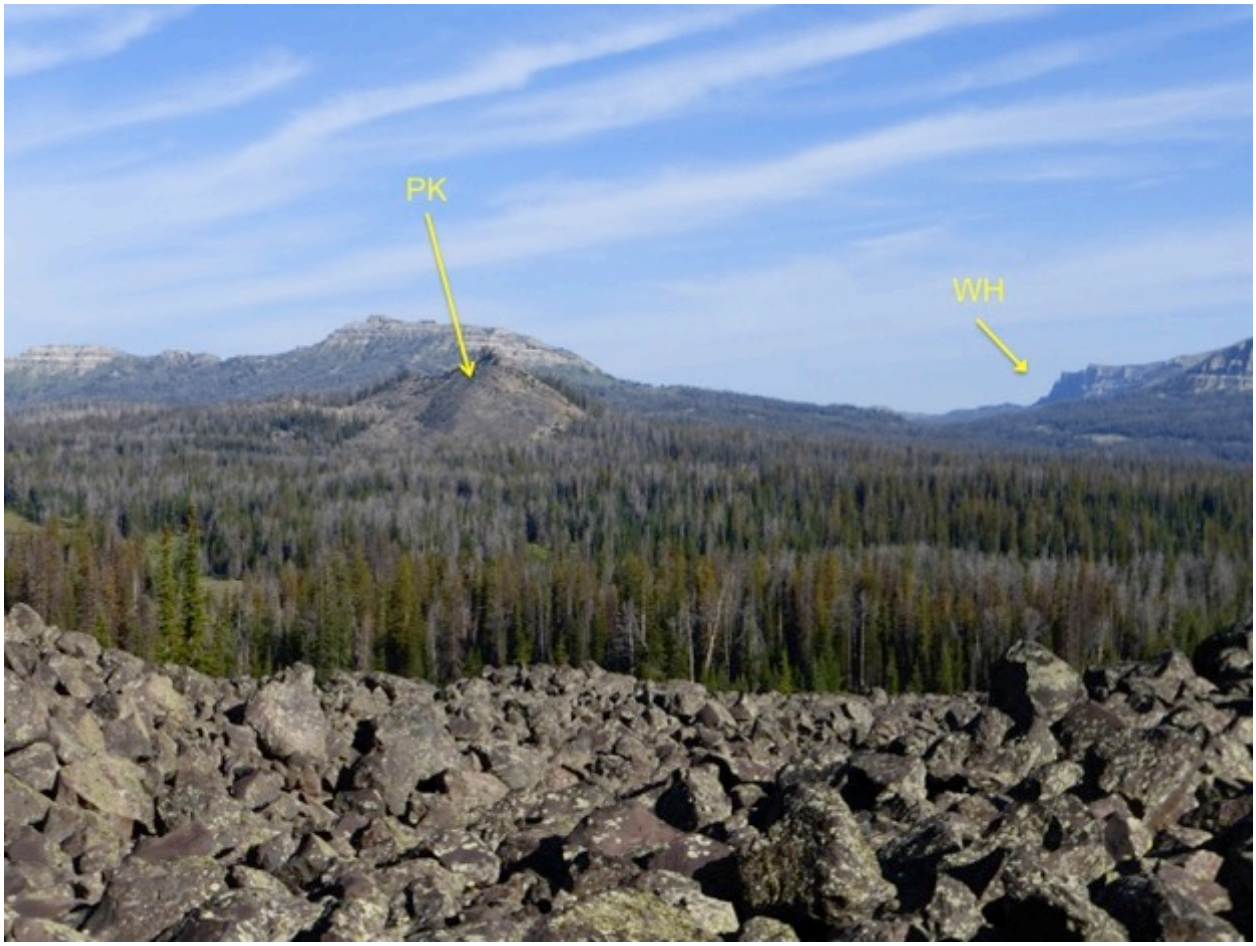

Figure 1-2 Pilot Knob and Wildcat Hill

View facing northwest showing Pilot Knob (PK) approximately 2 km away and Wildcat Hill (WH) approximately 15km away. Wildcat Hill sits at the base of the bedded cliffs that make up Absoraka volcanics.

1.2 Rare Earth Elements

In recent years, rare earth element (REE) research and interest have increased substantially. Modern technology relies heavily on REEs for vital components in jet turbines, batteries, magnets, conductive materials, and other objects related to "hi-tech" industry. However, lack of production in the United States has led to dependency on foreign countries to meet its needs. China in particular currently produces >90% of the world's REE supply (Kynicky, et al. 2012), essentially creating a monopoly on the global market. For these reasons—and because of the current limited supply of known REE deposits—further research and exploration in this subject is critical to the future global economy and is in the strategic interests of the United States.

1.2.1 Rare Earth Elements in Geologic Settings

According to the International Union of Pure and Applied Chemistry (IUPAC), the rare earth elements are composed of the lanthanide group of the periodic table of elements (atomic number 58-71), as well as yttrium, and scandium (Cornell, 1993). Although REEs are geologically common considering the geologic bulk composition of the Earth's crust, typically ranging from 150-220 ppm, they are rarely concentrated into economically mineable deposits (Long, et al. 2010). The 14 lanthanides (Figure 1-3) can be subdivided using their atomic numbers to differentiate between light rare earth elements (LREEs) and heavy rare earth elements (HREEs) by classifying La through Gd as LREEs and Tb through Lu as HREEs (Mariano and Mariano, 2012). For geologic purposes, however, Sc and Y are often not included in the list of REEs, because of subtle differences in their geochemical behavior relative to the more coherent lanthanide group.

Economic REE deposits can be either primary or secondary. Primary deposits are usually varieties of igneous rocks, such as carbonatites and alkaline rocks. Secondary occurrences include placer deposits and residual deposits formed from the weathering of primary deposits (Long, et al. 2010). For igneous REE deposits, these normally occur in intracontinental, anorogenic, extensional settings formed either by pull-apart tectonics or asthenospheric upwelling (Charkmourodian and Wall, 2012)

Currently, ~270 minerals are known to include these elements as a primary component of their crystal structure and chemical formulas, although most in uneconomic concentrations. The

most common mineral types are silicates (43% of all REE minerals), carbonates (23%), and phosphates and oxysalts (14%). There are currently 50 advanced REE exploration projects active outside of China, 20 of which are carbonatite igneous deposits and at least 13 projects are focused on alkaline silicate rocks (Chakhmourodian and Wall, 2012). Figure 1-4 provides a list of common REE-bearing minerals.

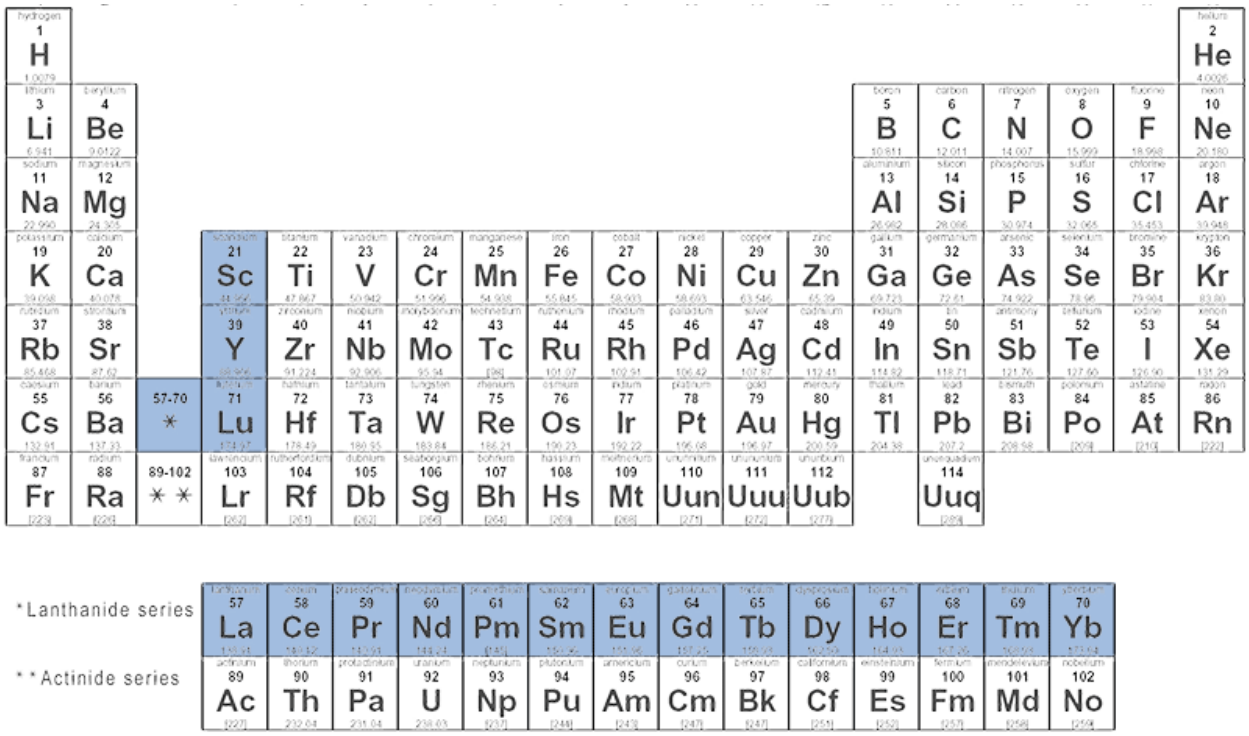

Figure 1-3 The rare earth elements

Rare earth elements shown in blue. For geologic purposes, Sc and Y are regularly disregarded. Light rare earth elements (LREE) are La – Gd and heavy rare earth elements (HREEs) are designated Tb – Yb. This study focuses primarily on three LREEs: La, Ce, and Nd (Dobransky, 2013)

Mineral	Chemical Formula[a,b]	REE as primary or accessory constituents
Allanite[c]	$Ca(Ce,La,Y,Ca)Al_2(Fe2+,Fe3+)(SiO_4)(Si_2O_7)O(OH)$	Minerals with REE as essential constituents
Ancylite	$Sr_3(Ce,La,Dy)_4(CO_3)_7(OH)_4 \cdot 3H_2O$	
Bastnasite	$(Ce,La,Y)CO_3F$	
Brannerite	$(U,Ca,Y,Ce)(Ti,Fe)_2O_6$	
Brockite	$(Ca,Th,Ce)PO_4 \cdot H_2O$	
Burbankite	$(Na,Ca)_3(Sr,Ba,Ce)_3(CO3)_5$	
Calkinsite	$(Ce,La)_2(CO_3) \cdot 4H_2O$	
Cerianite	$(CeTh)O_2$	
Carbocerianite	$(Ca,Na)(Sr,Ce,Ba)CO_3$	
Euxenite	$(Y,Er,Ce,U,Pb,Ca)(Nb,Ta,Ti)_2(O,OH)_6$	
Ewaldite	$Ba(Ca,Y,Na,K)(CO_3)_2$	
Fergusonite	$(Y,Er,Ce,Nd,La,Fe)(Nb,Ta,Ti)O_4$	
Gadolinite	$(Y,Ce,La,Nd)_2FeBe_2Si_2O_{10}$	
Mckelveyite	$Ba_3Na(Ca,Sr,U)Y(CO_3)_6 \cdot 3H_2O$	
Parisite	$Ca(Ce,La)_2(CO_3)_3F_2$	
Monazite	$(Ce,La,Y,Th)PO_4$	
Rhabdophane	$(Ce,La,Nd)PO_4 \cdot H_2O$	
Samarskite	$(Y,Ce,U,Ca,Th,Fe)(Nb,Ta,Ti)_2(O,OH)_6$	
Synchysite	$(Ce,La,Nd,Y)Ca(CO_3)_2F$	
Xenotime	YPO_4	
Apatite	$Ca_5(PO_4)_3(F,OH,Cl)_3$	Minerals with REE as accessory constituents
Columbite-Tantalite	$(Fe,U,Ca)(Nb,Ta)O_4$	
Fluorite	CaF_2	
Huttonite-thorite	$ThSiO_4$	
Pycrochlore-microlite	$(Na,Ca)_2(Nb,Ta,Ti)O_6(OH,F)$	
Sphene	$CaTiSiO_5$	
Zircon	$ZrSiO_4$	

Figure 1-4 Common REE-bearing minerals (Sutherland et al., 2013)

Common REE bearing minerals, including minerals with primary and accessory REE constituents.

1.2.3 Alkaline Igneous Deposits

The term "alkaline" can encompass a wide range of igneous rocks but, simply defined, are rocks deficient in SiO_2 relative to Na_2O, K_2O, and CaO (Verplanck and Van Gosen, 2011). The chemistry of alkaline rocks can vary extensively, making it difficult to classify certain deposits simply as alkaline. For example, silica concentrations can range from nearly 0 wt. % in some carbonatites to approximately 65 wt. % in more siliceous rocks such as trachyandesite (Raymond, 2007). Instead, several sub-categories have been developed, including carbonatites and peralkaline rocks, the two most common alkaline rock types known to host rare earth oxides (REOs).

1.2.3.1 Carbonatites

Carbonatites are igneous rocks containing >50% of primary carbonate minerals, such as calcite and dolomite (Chakhmouradian and Wall, 2012). They can be subdivided into a) calcite-carbonatite, b) dolomite-carbonatite, c) ferrocarbonatite, and d) natrocarbonatites (Streckeisen, 1979). Mountain Pass, California, perhaps the best-known domestic source of REEs in the United States, is a carbonatite REE deposit that has been produced since 1954. Currently Mountain Pass is the second largest REE deposit in the world behind Bayon Obo, China (Kanazawa and Masaharu, 2006). The Mountain Pass REE ore body is contained within the Sulphide Queen carbonatite (Castor, 2008), a sill approximately 75m thick. This and other regionally related subordinate carbonatite bodies are always associated with shonkinite, syenite, and granite, which have shown indications (with the support of similar ages and mineralogy) that these bodies have a cogenetic origin from an alkaline magma source (Mariano and Mariano, 2012).

Bayan Obo, China, discovered in 1927, is the world's largest REE project, having been in production since 1957 (Tse, 2011). Considered a carbonatite, studies have also shown that Bayan Obo may have formed due to hydrothermal activity and that the rare earth bearing minerals are closely associated with the high grade iron ore also mined at the location (Kanazawa and Masaharu, 2006). Hydrothermal REE deposits form via the movement of fluids, usually related to magmatic events. REEs can be sufficiently concentrated by fractional crystallization during hydrothermal activity to form REE-rich minerals (e.g. apatite). Although most carbonatite deposits are intrusive, there are a few extrusive examples, most notably

Oldoinyo Lengai volcano located in northern Tanzania (Woolley and Church, 2005). Additional REE carbonatite intrusives include the Bear Lodge Carbonatite in WY, USA; Maoniuping, China; and Mount Weld, Australia (Kanazawa and Masaharu, 2006). The most common REE-bearing minerals associated with carbonatites are bastnaesite and ancylite (Kanazawa and Masaharu, 2006).

1.2.3.2 Peralkaline Deposits

There are two primary types of peralkaline REE deposits: [1] deposits in peralkaline, layered complexes and [2] deposits in veins or dikes associated with the peralkaline intrusions. As a whole, the parental magma for those complexes hosting REE mineralization is generated as a partial melt of metasomatized mantle material. This has been interpreted as evidence that the initial melt is the source of the REE-bearing minerals (Verplank and Van Gosen, 2011).

Currently there are no actively producing projects focusing on peralkaline intrusions, but there are numerous prospects in various stages of development. Bokan Mountain, located in the southern part of Prince of Wales Island, Alaska, is an example of a peralkaline deposit and, according to a 2010 USGS report on REEs, has an estimated resource of 6.8 million tons of ore with an average of 0.264 wt. % REEs. Of this, approximately one third is yttrium (Long et al., 2010). Many of the peralkaline deposits like Bokan Mountain are under investigation for economic viability and estimated tonnage. As technology advances, these prospects will likely become profitable REE productions.

1.2.4 Other Deposits

There is a wide range of other REE deposit types including sedimentary deposits (i.e. placers and weathered residual deposits), secondary deposits, and others. The ion-adsorption clays located in South China are a prime example of this. As a deeply weathered residual deposit, these ion-adsorption clays currently have combined estimated resources of >1 million tons, all formed from lateritic weathering of felsic rocks. Although these have relatively low ore grades (0.05 – 0.2 wt. % REOs), they are relatively easy to extract and thus can be very profitable (Kynicky et al., 2012)

1.3 Geologic Background

1.3.1 Wind River Basin, Laramide uplift, and Structural Inversion

Regionally, the study area is located on the western extremity of the Upper Wind River Basin (UWRB). The Wind River Basin is a west to east trending, asymmetrical, intermontane basin located in northwest Wyoming. The basin is fault-bounded by Laramide uplifts including the Owl Creek Mountains to the north, Wind River Mountains to the west and south, and the Casper Arch to the east (Fox and Dolton, 1995). Pilot Knob and Wildcat Hill both intrude through Eocene sedimentary and volcaniclastic strata present in the UWRB (e.g., Wiggins Formation).

During the Paleozoic through Mesozoic, Wyoming was part of the foreland bordering the Cordilleran geosyncline in the east (Keefer, 1970). The Laramide uplift refers to the period of basin and range formation of the Rockies and can encompass a wide range of dates depending on which regional location is considered. Basin development of the Wind River Basin is dated at late Cretaceous to early Eocene time (Love, 1960); uplift of the surrounding mountain ranges is thought to have occurred over a similar timeframe (Keefer, 1970), along with down-warping of the basin trough and broad doming of parts of the peripheral areas (Keefer, 1965) (Figure 1-7). Throughout this entire period, widespread crustal deformation occurred throughout Wyoming, with major thrust and reverse fault zones forming the large mountain ranges seen today (Love, 1960); this also is what formed the basinal regions throughout Wyoming. According to Blackstone (1990), an extensive, severely glaciated surface, created after the deformation, covers the study areas. Glacial erratics are observed around Lava Mountain, a young volcanic edifice with associated lavas just ~2 km southeast of Pilot Knob. These are believed to be associated with the earliest period of glaciation recognized in the area, a large ice mass dating back possibly as early as 480,000 years (Obradovich, 1978). This period of glaciation is believed to be the cause of most of the erosional features found on Pilot Knob and the surrounding area.

1.3.2 Yellowstone Volcanism

The Yellowstone volcanic field is a compositionally bimodal, but predominately rhyolitic, volcanic system that has erupted approximately 6,000 km^2 over the past 2 m.y. (Christiansen et al, 2002). The most commonly accepted explanation for Yellowstone volcanism is that the North American Plate migrated west to east over the Yellowstone hotspot, a stationary

mantle plume over the last ~17 Ma (Pierce and Morgan, 1992). The trace of the plume of the plume extends from northern Nevada through Idaho to Wyoming, with the hotspot currently located primarily under Yellowstone National Park. Significant hydrothermal and tectonic activity has been documented here as a result. The Yellowstone plateau volcanic field is characterized by three caldera-forming silicic eruptions of the Huckleberry Ridge tuff (2.1 m.y.), Mesa Falls tuff (1.3 m.y.), and Lava Creek tuff (0.64 m.y.), as well as volumetrically minor rhyolite and basalt lavas before and after the caldera-forming events (Christiansen, 2001).

1.3.3 <5 Ma upper Wind River Basin volcanism, including Lava Mountain

~2 km southeast of Pilot Knob is an intermediate-composition volcano, Lava Mountain, where the youngest lava has been dated at 0.48 ± 0. 06 myr (Obradovich, 1978; Downey et al., 2014). Both Lava Mountain and Pilot Knob are part of a regionally extensive group of <4 Ma volcanoes and intrusive bodies in the UWRB that are relatively unstudied with respect to their petrogensis and tectonic affinity (Downey et al., 2014). Compositionally similar and slightly older igneous rocks in the Jackson Hole, WY region have been suggested to form via melting of Archean lithosphere based on Sr and Nd isotope signatures (Adams, 2014). However, more work is needed to decipher how the UWRB volcanics, including Pilot Knob and Wildcat Hill, are petrogenetically related.

Crescent Mountain, located approximately 25 km northeast of Lava Mountain, is a volcano in the Upper Wind River Basin region and forms an arcuate ridge of massive intermediate composition lavas (Prostka et al., 1979) and yields a K-Ar age on one flow of 3.6 m.y. (Blackstone, 1966). Also, Spring Mountain, located approximately 20 miles east of Lava Mountain, exhibits presumably young (e.g., younger than Eocene Absaroka volcanics) volcanism as well as normal faulting hypothesized to be related to the recent extension in the region.

1.3.4 Leucite Hills

The Leucite Hills, located in Southwest Wyoming (Figure 1-5), are 22 volcanic occurrences that are mostly oriented northwest – southeast. These occurrences are parallel to the Farson Lineament and Masstrichtian thrust fault, which are products of the Laramide Orogeny and consist of 3.0- 1.89 Ma lamproites cutting through the northern portion of the Upper Cretaceous Rock Springs Uplift (Mirnejad and Bell, 2006). Lamproites are potassic, alkaline, igneous rocks and are also known to have the potential of carrying diamonds and substantial REE-enrichment (Mitchell and Bergman, 1991). The lamproites present at Leucite Hills can be classified into four distinct groups: phlogopite lamproites (both diopside-leucite-phlogopite lamproites and diopside-sanidine-phlogopite lamproites), madupitic lamproites, and transitional madupitic lamproites (Mirnejad and Bell, 2006). The Leucite Hills lamproite shows a wide range of SiO_2 concentrations (41.02 to 55.82 wt. %) and other major element data are consistent with alkaline igneous rocks (Mernejad and Bell, 2006). It was discovered that the madupitic lamproites contained the highest MgO and the lowest SiO_2 values and the phologopitic lamproites contained higher SiO_2 (Mirnejad and Bell, 2006). These findings are suggestive of two separate magmatic events forming the Leucite Hills (either two distinct magma sources/events or two separate episodes of magmatism). Additionally, LREE concentrations were highest in the madupitic lamproites (Mirnejad and Bell, 2006). Of the mineralogy listed by Mirnejad and Bell (2006), apatite can occur in both the groundmass and as a phenocryst and is assumed to be the primary host for LREE enrichment in the Leucite Hills.

The cause of the Leucite Hill magmatism is quite complex and presumed to be sourced from lithospheric mantle. Based on LREE content, bulk geochemistry, and Sr-Nd-Pb isotopic data, the Leucite Hills lamproites are presumed to be the result of a three-stage development: (1) major melt removal from Wyoming upper mantle leaving depleted sub-continental lithosphere (2.8 Ga); (2) ancient metasomatism of the sub-continental mantle related to crustal subduction (>1 Ga); and (3) recent metasomatism of the sub-continental lithosphere during mantle upwelling, likely due to shallow-slab Laramide subduction (<100 Ma) (Mirnejad & Bell, 2006).

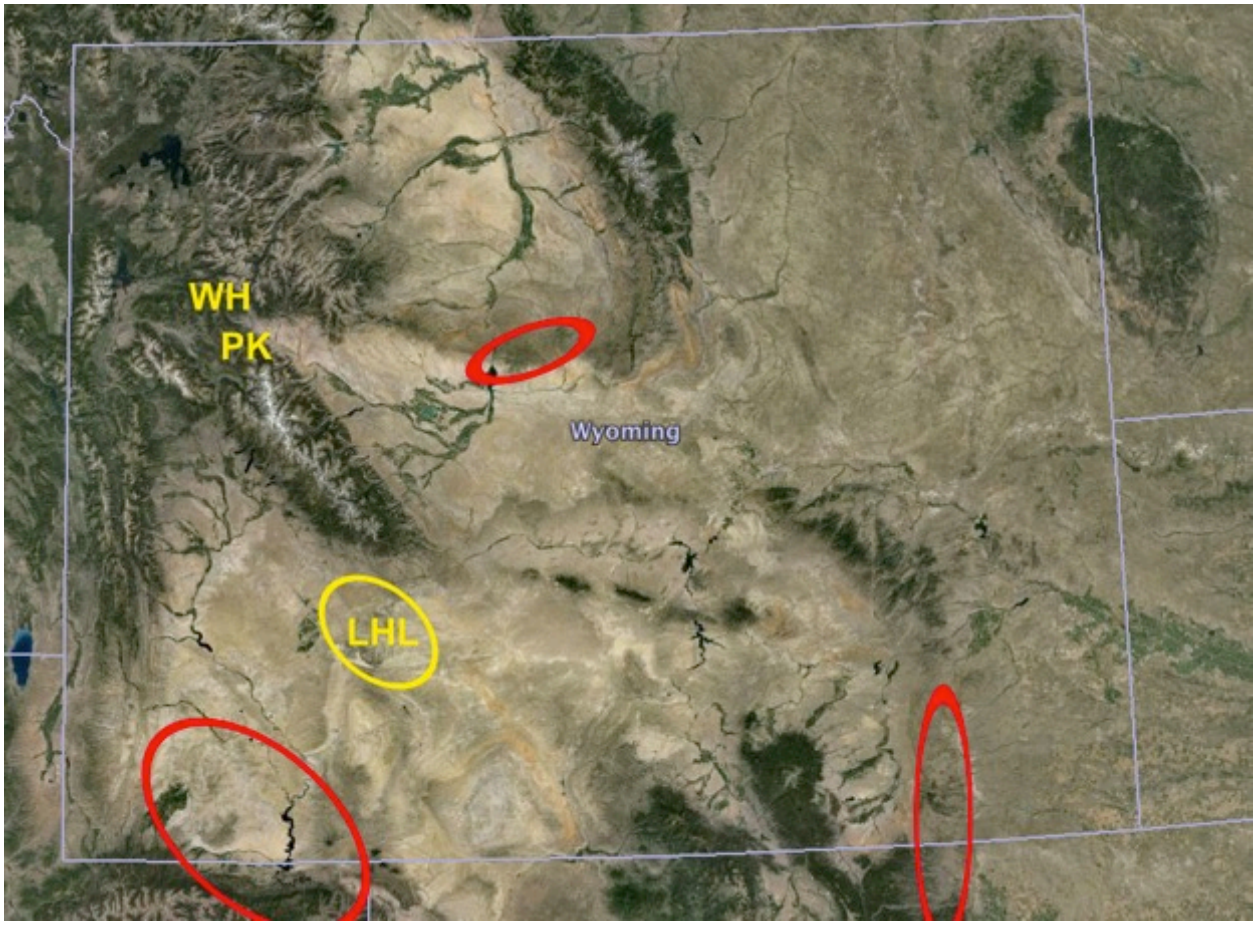

Figure 1-5 Wyoming satellite image showing Leucite Hills, kimberlite tracers, and study area.

Google Earth Satellite image of Wyoming. PK, Pilot Knob; WH, Wildcat Hill; LHL, Leucite Hills; red circles indicate areas of kimberlite or diamond indicator minerals (data adapted from Hausel, 2014).

1.3.5 Extensional Tectonism

Normal faulting is present in northwest Wyoming and has been linked to extensional tectonism in this part of the North American plate and the effects of crustal doming over the Yellowstone hotspot and/or regional Basin and Range extension seen throughout Idaho and Wyoming (Christiansen et al., 2002; Anders, et al., 2009). Figure 1-1 shows a normal fault zone northwest of the study area. Many of these faults trend approximately north-south. Based on regional geologic and structure maps (Figure 1-7), it is likely that these faults project further south into the study area. Regional faulting and igneous complex outcrops, such as dikes, all tend to trend northwest, providing evidence of tectonic activity. It is likely that Wildcat Hill, Pilot Knob, Lava Mountain and other local dikes lie on fault splays or lineaments from these normal faults, as shown in this study (Figure 1-6, Figure 1-7).

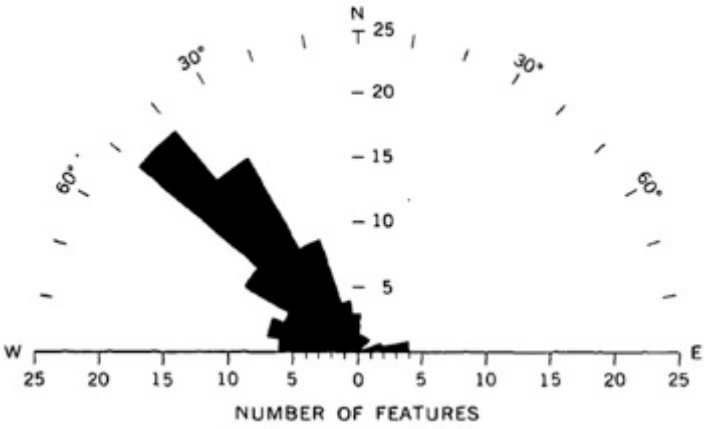

Figure 1-6 Diagram showing structural trends in the Wind River Basin
Image shows 92 structural features (anticlines, faults, and major synclines) in the Wind River Basin (Keefer, 1970) showing regional structure trending approximately 315 degrees.

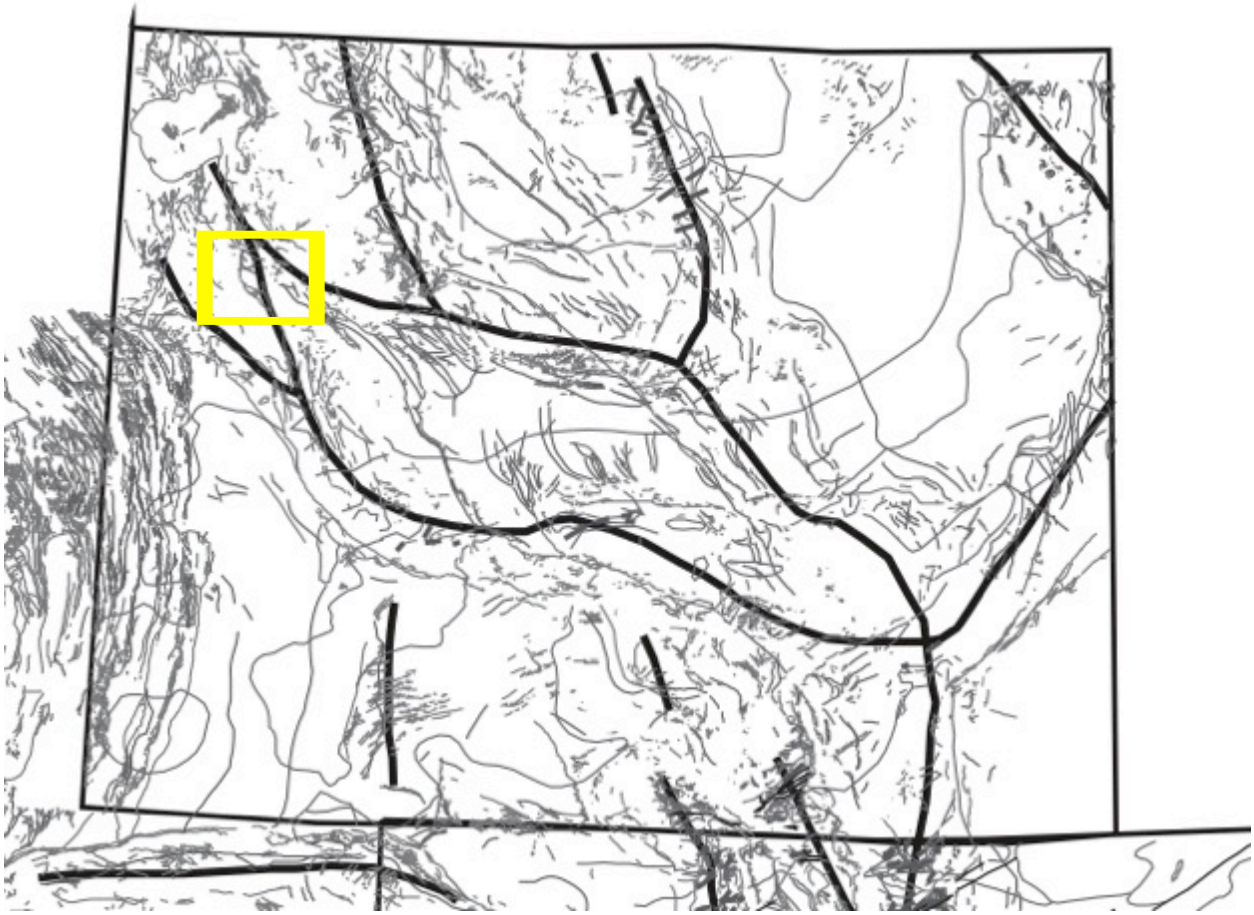

Figure 1-7 Structure map of Wyoming

Structural geology map of Wyoming (adapted from Erslev and Koenig, 2009). Bolded lines indicate major arch features; gray lines indicate faults/folds; yellow box indicates study area. Extensional related faulting generally trends northwest – southeast, in line with study area as seen in figure 1-1.

Chapter 2 - METHODOLOGY

2.1 Field Work

The project and sampling location focuses on an ~6 km^2 area encompassing Pilot Knob and ~2 km^2 area encompassing Wildcat Hill (Figure 1-1). Samples were obtained systematically from each study area. Three samples (ZD14-2, ZD14-5, and ZD14-6) were obtained from Pilot Knob and complimented by one additional sample (MB13-2) provided by M. Brueseke from fieldwork conducted at the same location in 2013. Detailed geologic mapping was conducted while sampling Pilot Knob. Notably, a dike was observed at the top of Pilot Knob trending approximately NNE (Figure 2-2). Access to Pilot Knob was obtained via Moccasin Basin Rd from highway 26.

Two representative samples were then obtained from Wildcat Hill (ZD14-19a and ZD14-19b) representing the two distinctive lithologies identified at the outcrop. The intruded strata are Eocene Wiggins Formation. Access to Wildcat Hill was achieved via a trail that lies off of Highway 26, approximately one mile west of the continental divide.

To help determine whether Pilot Knob represents more than one magma body, as well as to identify any unique characteristics, detailed geologic mapping of bedrock was conducted at a scale of 1:6,000 covering Pilot Knob and the surrounding area (Figure 2-1). Attention was given to geologic contacts, formation types, structural features, and surrounding geology. Mapping and rock sampling were extended outward from Pilot Knob to search for evidence of hydrothermal alteration (e.g., alkali metasomatism or fenitization) of surrounding rocks; typically the REE are more concentrated in such contact aureoles than they are in the intruded magma (Verplanck and Van Gosen, 2011). Fieldwork did not encounter an "alteration halo." Additionally, Wildcat Hill was studied at reconnaissance scale to help identify any physical, geochemical, and structural similarities to Pilot Knob; no mapping was performed here, although it was readily apparent that the intrusion penetrated Wiggins Formation strata. The only similarities are that both of these locations are igneous intrusive bodies that cut Eocene sedimentary strata.

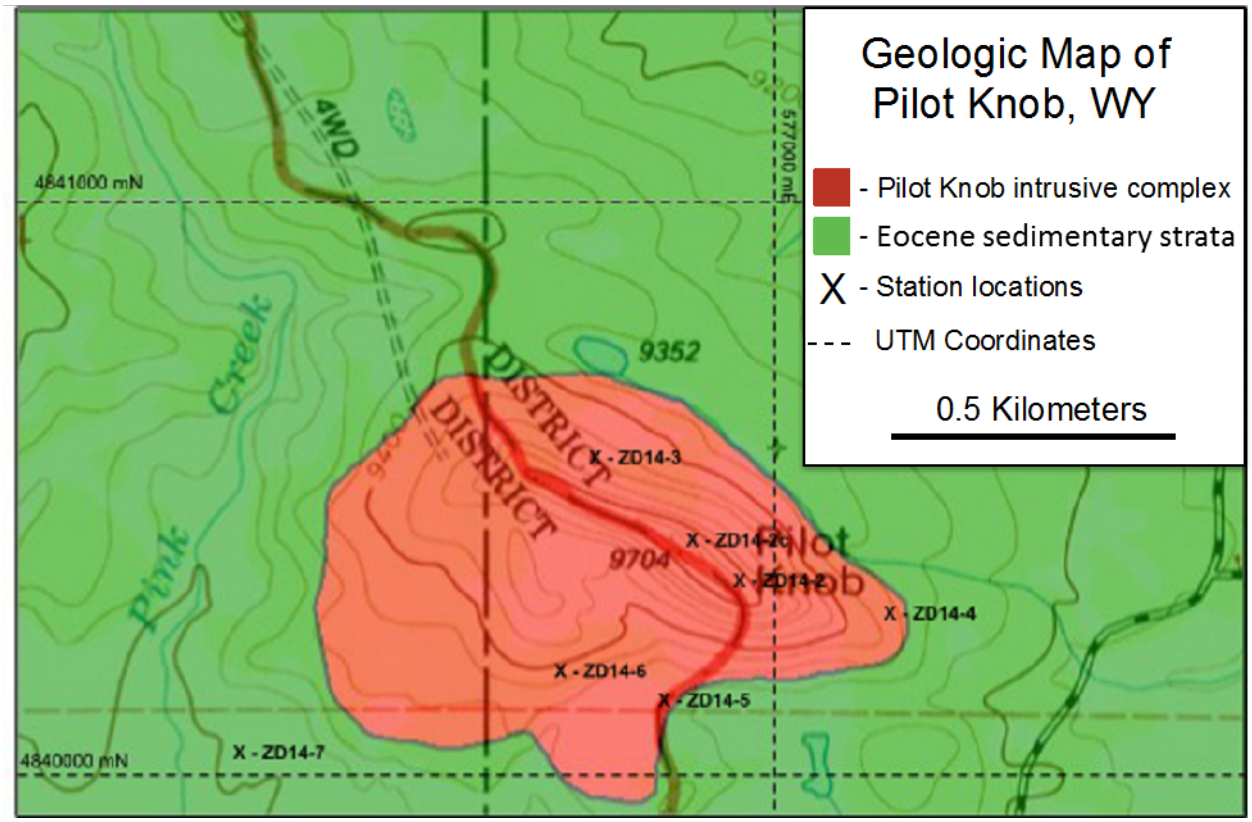

Figure 2-1 Geologic map of Pilot Knob, WY

Geologic map overlay on top of the U.S.G.S. Lava Mountain 1:24000 topographic quadrangle. Pilot Knob intrusive complex shown in red; Eocene sedimentary strata is shown in green. Boulder fields litter the southern and northern portions of the Pilot Knob boundaries. Samples collected correspond with station numbers and locations listed.

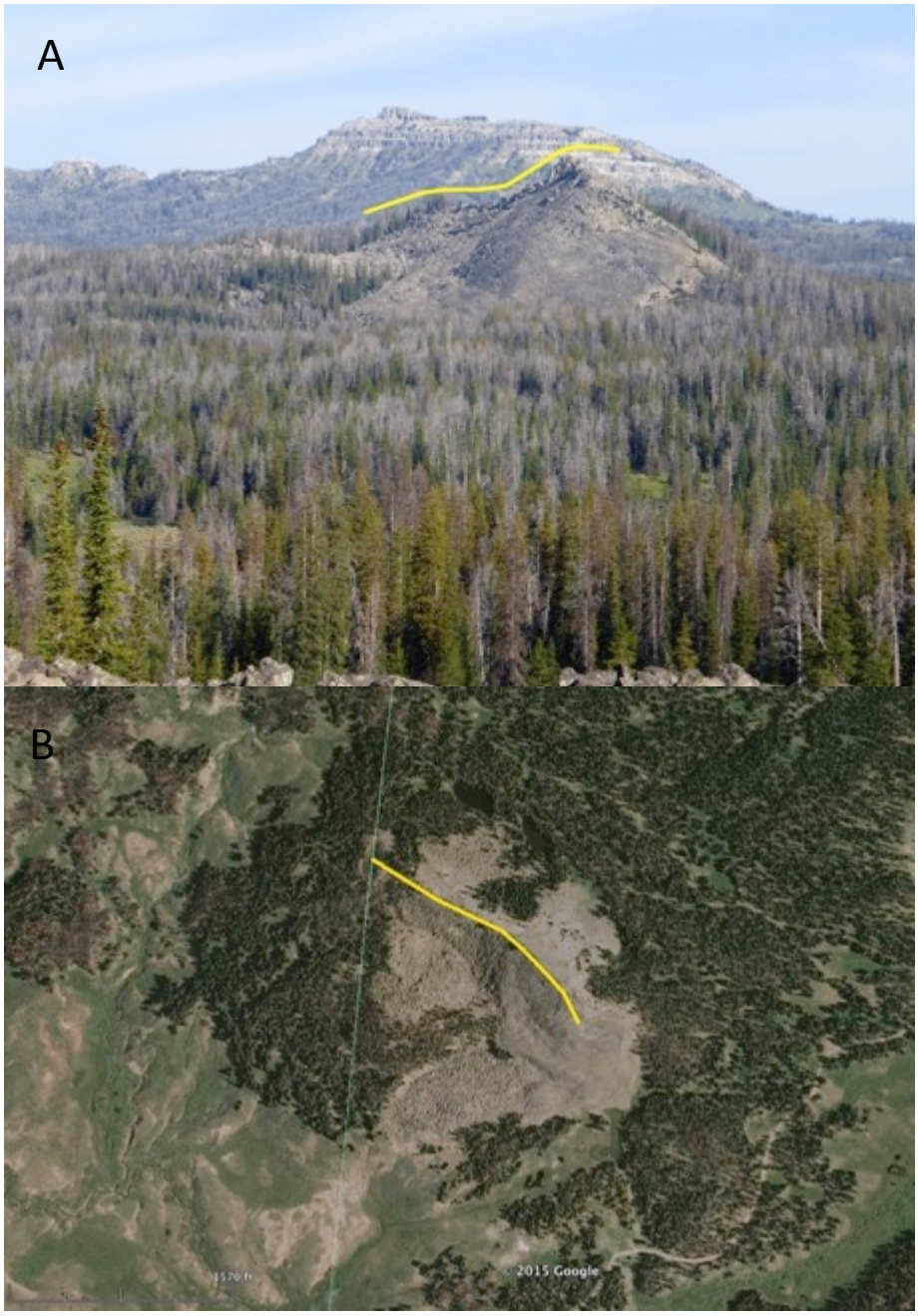

Figure 2-2 Pilot Knob

(A) Photo displaying Pilot Knob, looking northwest from Lava Mountain (Figure 1-1). Seen at the top of Pilot Knob is what appears to be a dike feature (highlighted in yellow). Boulder fields surround it on all sides, presumably created by glacial erosion.

(B) Google Earth satellite image of Pilot Knob. Yellow line indicates presumed dike location, trending northwest. Boulder fields can be seen on the southern edges of Pilot Knob.

Figure 2-3 Wildcat Hill

Photo looking SW at Wildcat Hill, showing volcaniclastic strata (background cliffs and subdued terrain in foreground) surrounding the intrusion. Yellow line indicates approximate intrusion boundary.

2.2 Lab Work

2.2.1 Petrography

Rock thin sections were obtained via contract with Spectrum Petrographics. Petrographic descriptions of the thin sections were performed at Kansas State University using a Nikon petrographic microscope. A Nikon camera and SCOPE software were used to develop photomicrographs of the samples; these data were used to help refine field-based physical descriptions of mapped and sampled units, as well as allow for the preliminary identification of REE-bearing minerals and any hydrothermal alteration in mapped units. Point counting targeting approximately 800 counts per slide and averaging 758 counts per slide, was also conducted to provide better mineralogical constraints and bulk compositions on the study area. The variation in points per slide is due to variations in thin section sample sizes. A full description of thin section analyses is listed in Appendix A.

2.2.2 Bulk Rock Geochemistry Sample Preparation

Samples were processed and prepared at Kansas State University. Approximately fist-sized field samples were split then crushed with a Rocklabs hydraulic splitter/crusher. Tungsten carbide "knife" plates were first used for splitting, and the samples were condensed into approximately three cm cubes while any alteration and weathered faces were carefully removed. Any remaining weathering and alteration were then removed using a diamond blade rock saw and grinding wheel. Pieces of sample were then selected for thin section billets before the remainder was crushed further. Tungsten carbide flat plates were then used to crush/pulverize the samples into <5 mm gravel. To ensure homogeneity, a cone and quartering method was used to select 20 ml of sample for final powdering. Final pulverization of the sample into clay-sized particles was then completed using a Spex Industries aluminum oxide shatter box. The sample was then placed in a 30 ml glass container to be sent for ICP-OES and ICP-MS analysis at Miami University and MC-ICP-MS at Washington State University.

2.2.3 Bulk Rock Geochemistry

Bulk rock geochemical data were used to fully characterize the Pilot Knob and Wildcat Hill samples, including the degree of bulk rare-earth element enrichment. Samples selected for geochemical analysis were chosen based on geological mapping, with the intention being to

constrain the compositional variability of Pilot Knob and to determine whether or not Pilot Knob and Wildcat Hill are enriched in REEs.

Inductively coupled plasma optical emission spectrometry (ICP-OES) was performed for major element bulk geochemistry analysis. Samples ZD14-2 and ZD14-19a were analyzed. 200mg of sample were collected and fused with 600 mg of $LiBO_2$ which was then passed through a cation resin to isolate different elements and then dissolved in 20 ml of 0.3N HNO_3. Samples were then analyzed by Agilent ICP-OES using a Cetac ultrasonic nebulizer.

Inductively coupled plasma mass spectrometry (ICP-MS) was performed for REE analysis on six samples: ZD14-2, ZD14-5, ZD14-6, MB13-2, ZD14-19a, and ZD14-19b. 75 mg of a 3:2 mixture of sodium tetraborate and potassium carbonate, respectively, was used as a flux and mixed with 50 mg of powder from each sample. The samples were then heated to 950° C for 30 minutes in a graphite crucible. After the sample cooled, it was them moved to an acid-washed, low density, polyethylene bottle containing 125 ml of 1% HNO_3. The samples were dissolved overnight and then analyzed using a Varian "Red Top" ICP-MS. Calibration and standardization utilized a 100 ppb solution of Ge, Re, Bi, and In.

2.2.4 Electron Microprobe

Electron microprobe analysis was performed at Colorado University in March, 2015, on a JEOL JXA-8600 equipped with four wavelength-dispersive spectrometers and one energy-dispersive spectrometer. Analyses were acquired using the dQuant interfaced with the Geller microprobe automation. Standards used range from simple silicates and oxide end-member compounds to primary silicate standards recognized throughout the analytical community. More information can be found here: http://geode.colorado.edu/~jallaz/index.php?page=microprobe&tab=other. ZD14-5, ZD14-6, and ZD14-19a were chosen for analysis and were sputter-coated with carbon. Pyroxene, feldspar, mica, and apatite compositions were then analyzed and are listed in Appendix C. Alteration was noted on many of the crystals and line scans and rim/core data points were collected of selected altered crystals. Representative photos of crystals analyzed as well as their location within each thin section are listed in Appendix C. General parameters used were 20-25 nA with a 5-10 μm spot size. Pyroxene crystals used a focused bean (~1μm) and apatite crystals analyzed for REE content used 30 nA.

Mineral recalculations were performed in Microsoft Excel and the relevant formulae used are listed in Apendix C. Mica mineral recalculation found OH and H_2O values not recorded by the electron microprobe based on a 12 oxygen basis. Total oxygen moles for each molecule detected were calculated and summed. The conversion factor was then calculated by dividing 12 oxygens by the total oxygen moles preset. OH was then calculated by accounting for F and Cl moles then multiplying by the conversion factor. H_2O was then calculated, providing an accurate 'total' amount for the analysis. All mineral recalculations were performed in MS-Excel. After all mineral recalculations were completed, spreadsheets (Appendix C) were created showing percentage of different end members. Average mineral compositions for Pilot Knob and Wildcat Hill are listed in chapter 3. IgPet software was then used to create ternary diagrams displaying these results.

2.2.5 Radiogenic Isotope Data

One sample was selected for isotope analysis: ZD14-2. Nd isotopes were analyzed at Washington State University using a ThermoFinnigan Neptune multicollector (MC)-ICP-MS. The effects of mass fractionation during calculations for Nd isotopes were corrected using $^{143}Nd/^{144}Nd = 0.7219$ and normalized to the Ames standard. Data was presented as two standard errors, with an average reproducibility of two standard deviations. The average reproducibility for $^{87}Sr/^{86}Sr$ on the NBS-987 standard was 0.00005, and reproducibility for $^{143}Nd/^{144}Nd$ on the Ames standard was 0.00002. Nd isotope ratios are reported corrected to 3.5 Ma. Overall Nd isotope procedures follow the methods outlined in Gasching et al., 2011.

Chapter 3 - RESULTS

3.1 Physical Characteristics of Pilot Knob and Wildcat Hill

Pilot Knob has a "fin" like structure at its peak trending northwest, which is interpreted as a dike (Figure 2-2). At the top of Pilot Knob, several locations were found showing horizontal, parallel fracturing that is a shallow intrusive texture caused by rapid cooling (Figure 3-1). Surrounding Pilot Knob are large boulder fields with boulders averaging approximately 2-3 meters in diameter. These boulder fields are presumed to be part of the glacial erosion referenced by Blackstone (1993).

Pilot Knob is a very resistant outcrop. Intruded strata are all sedimentary units and have created valleys and lows surrounding Pilot Knob, but the intrusion itself has remained as a steep outcrop surrounded by weathered and eroded boulders on all sides. Vertical cooling joints on the intrusive body itself have provided fractures that have been exploited by weathering, but many fresh surfaces exist at the top of the outcrop (Figure 3-1).

Wildcat Hill, although compositionally homogenous, was found to have two texturally distinct rock types present, consistent with a possible "outer" and "inner" portion of an intrusive body. ZD14-19a exhibited a vesicular and blocky texture, consistent with the interior of a hypabyssal intrusion (Figure 3-2). Large blocky fractures showing cooling patterns are also present throughout the outcrop. ZD14-19b exhibited a glassier texture, indicating it represents a portion of the intrusion margin chilled against the adjacent country rock, thus showing more rapid cooling.

Like Pilot Knob, Wildcat Hill intrudes relatively soft volcaniclastic sediments and outcrops in cliff-like formations. Weathered blocky boulders surround the western flank, deposited there by weathering and erosion. On a local scale, massive glacial cirques were noted surrounding the study area, leaving Wildcat Hill and the nearby Absoraka volcanic cliffs as an arête. In hand sample, the rock appears darker in color and looks basaltic. Wildcat Hill additionally exhibits columnar jointing, presumably related to its cooling history.

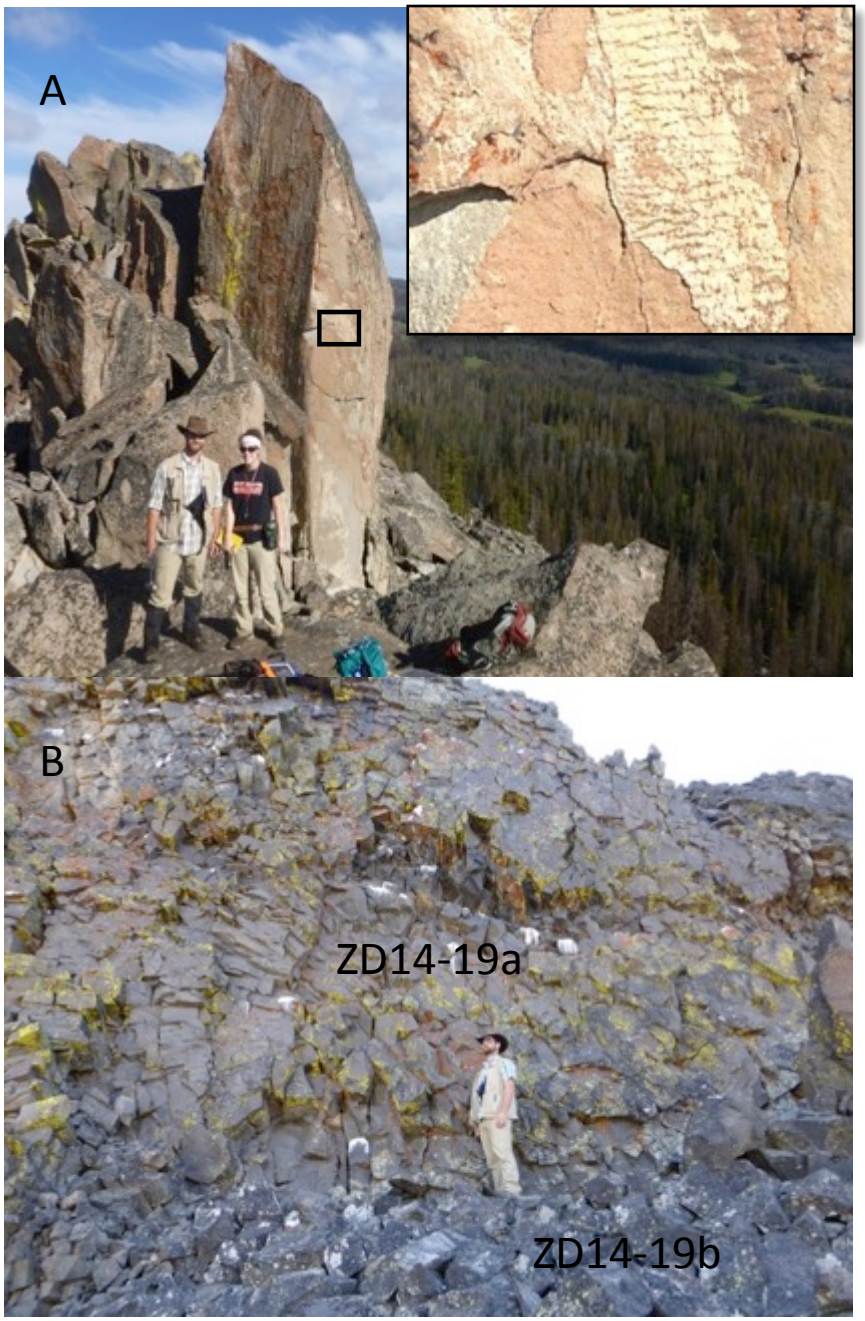

Figure 3-1 Cooling textures at Pilot Knob and Wildcat Hill

(A) Main image shows top of Pilot Knob. Inset is enlarged image showing horizontal cooling fractures seen in the vertical cooling joint in dike.

(B) Wildcat Hill outcrop showing vesicular, blocky outcrop (center of photo) like ZD14-19a and slightly glassier and darker, blocky outcrop (lower left portion of photo) like ZD14-19b. These textural differences likely indicate different cooling histories within the intrusion.

Figure 3-2 Wind River Fm and Wiggins Fm

(A) The intruded Eocene sedimentary strata in proximity with Pilot Knob. Cliff is ~ 5 meters tall. (B) Wiggins Formation volcaniclastic strata located to the west of Wildcat Hill. Hammer in center of photo is approximately 40 cm.

3.2 Petrography

Detailed petrographic descriptions of samples used in this study can be found in Appendix A. Petrographic analysis, consistent with geochemical results, showed several differences between Wildcat Hill and Pilot Knob. Pilot Knob samples all appeared fairly homogenous in texture and composition. All Pilot Knob samples were aphanitic coarse to medium grained rocks that average approximately 67.1% plagioclase, 14.5% clinopyroxene, 6.5% biotite, 6% orthopyroxene, and 6% apatite; the glassy portions of the Pilot Knob samples are hypothesized to be mesostatis (Figure 3-5). Some Pilot Knob samples exhibited a holocrystaline texture. Plagioclase is the dominant mineral phase present and occurs primarily as a groundmass phase where it is fine-grained (< 0.25mm), euhedral to subeuhedral, and exhibits strong carlsbad twinning. Some plagioclase phenocrysts were also noted (Figure 3-3c). Apatite crystals are often poikilitically enclosed within the plagiocase. Zoning is also evident in most plagioclase crystals, indicating crystal growth patterns. Clinopyroxene crystals range from 0.5 to 1.5 mm in size; they typically exhibit sieve and resorption textures and were noted in both phenocryst and groundmass phases. The poikilitic orthopyroxenes present do not appear as weathered as the clinopyroxene and are intergrown with plagioclase crystals as glomerocrysts. Biotites (Figure 3-3b) are 2-25mm in size throughout all Pilot Knob samples and exhibit strong resorption and subsequent weathering textures, appearing altered along the outer rims of most crystals. Trace amounts of zircon and amphibole were also noted in groundmass.

Pilot Knob rocks have been identified in this study as lamprophiric (Obradovich, 1978). Lamprophyres are porphyritic dyke-rocks that can be very heterogeneous in mineralogy and nature, but all seem to have the common characteristics of a late stage intrusion in an igneous event and the presence of amphibole or mica (primarily biotite or phlogopite) (Rock, 1977) as well as pyroxene in either a phenocryst or groundmass phase, while feldspar is restricted to the groundmass (Woolley et al., 1996). Many lamprophyres plot within the field of trachybasalt on a total alkalis vs. silica diagram (LeBas and Streckeisen, 1991), but this geochemical classification overlooks some of the distinctive petrographic features of lamprophyres. For this reason, lamprophyres are commonly classified on the basis of their mineralogy as much as on the basis of their geochemistry. While plagioclase is traditionally restricted to groundmass phase in lamprophyre classification, for the purpose of this study, Pilot Knob is still being classified as a

lamprophyre based on modal mineralogy because it fits the characteristics of lamprophyre as outlined in Le Maitre (2002) better than anything else and this classification is consistent with its bulk chemical composition.

Obradovich (1978) classified Pilot Knob as a particular type of lamprophyre known as a vogesite. A vogesite (Figure 3-6) contains primarily orthoclase with the predominant mafic minerals being hornblende, diopsidic augite, and olivine. However, for Pilot Knob, the hydrous mineral phase is exclusively mica rather than amphibole and its composition is primarily phlogopite with plagioclase > orthoclase (Figure 3-13). Therefore, the Pilot Knob intrusion can be classified, using Le Maitre (2002), as a kersantite (Figure 3-6).

Both samples from Wildcat Hill (ZD14-19a and ZD14-19b) appear homogenous in composition. Texturally there is a glassier variety at the outcrop scale . The Wildcat Hill (Figure 3-3d) intrusion is hypabyssal in origin, with more fine-grained textures than Pilot Knob. It consists of approximately 72.4% groundmass, 8.8% clinopyroxene, 8.5% plagioclase phenocrysts, 7.5% biotite, and 3.2% orthopyroxene. Plagioclase-dominated matrix within Wildcat hill consists of primarily < 0.1mm plagioclase crystals with some plagioclase phenocrysts up to 0.3mm. . Pyroxene crystals are approximately 0.5mm in size do not appear as weathered as Pilot Knob. No apatite was noted in Wildcat Hill.

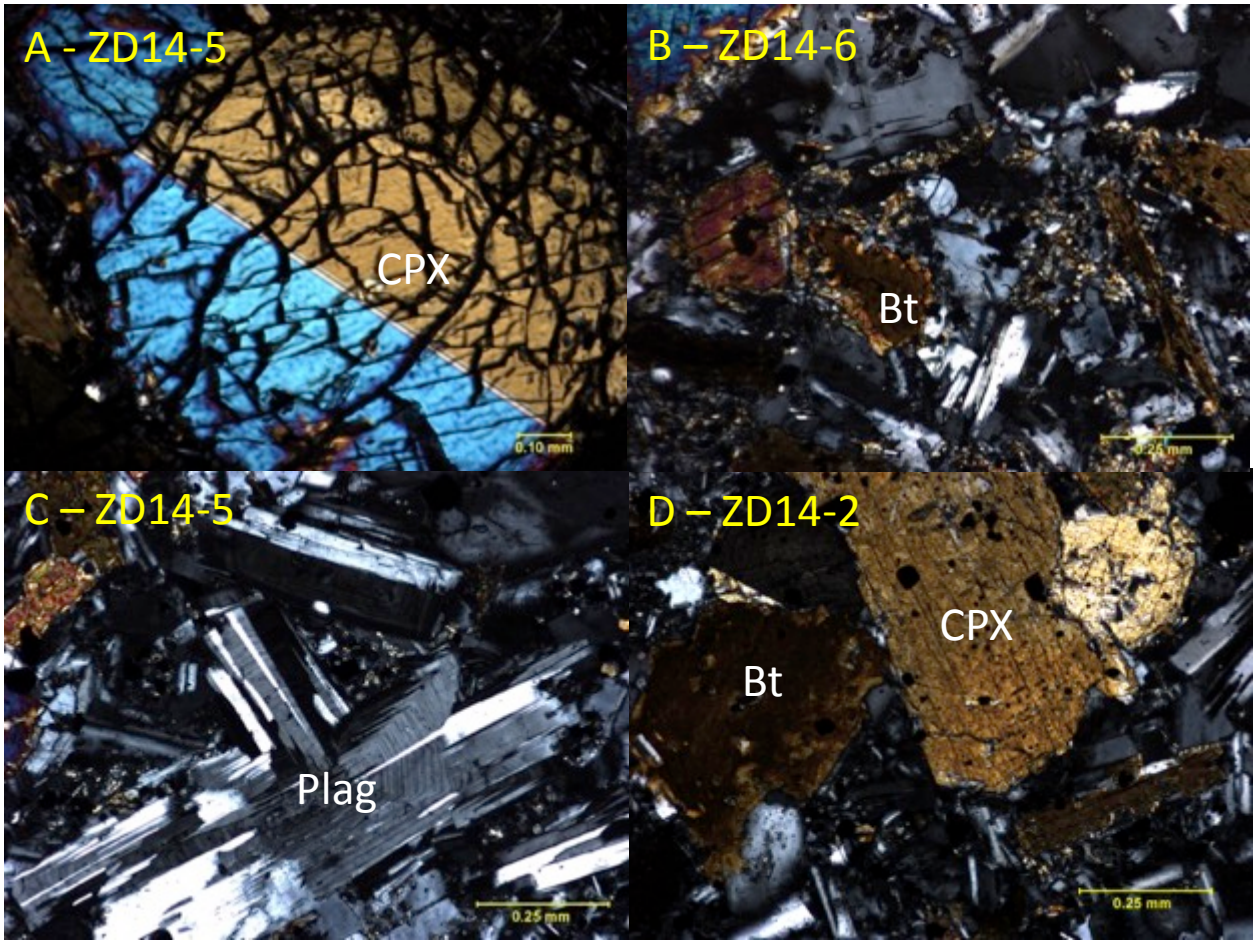

Figure 3-3 Pilot Knob thin section photomicrographs

All photos are in cross-polarized light at 10x magnification. [A] Zoned clinopyroxene [B] weathered biotite in plagioclase dominant matrix, [C] zoned and twinned plagioclase crystal, and [D] biotite. CPX = clinopyroxene; Bt = Biotite; Plag = plagioclase

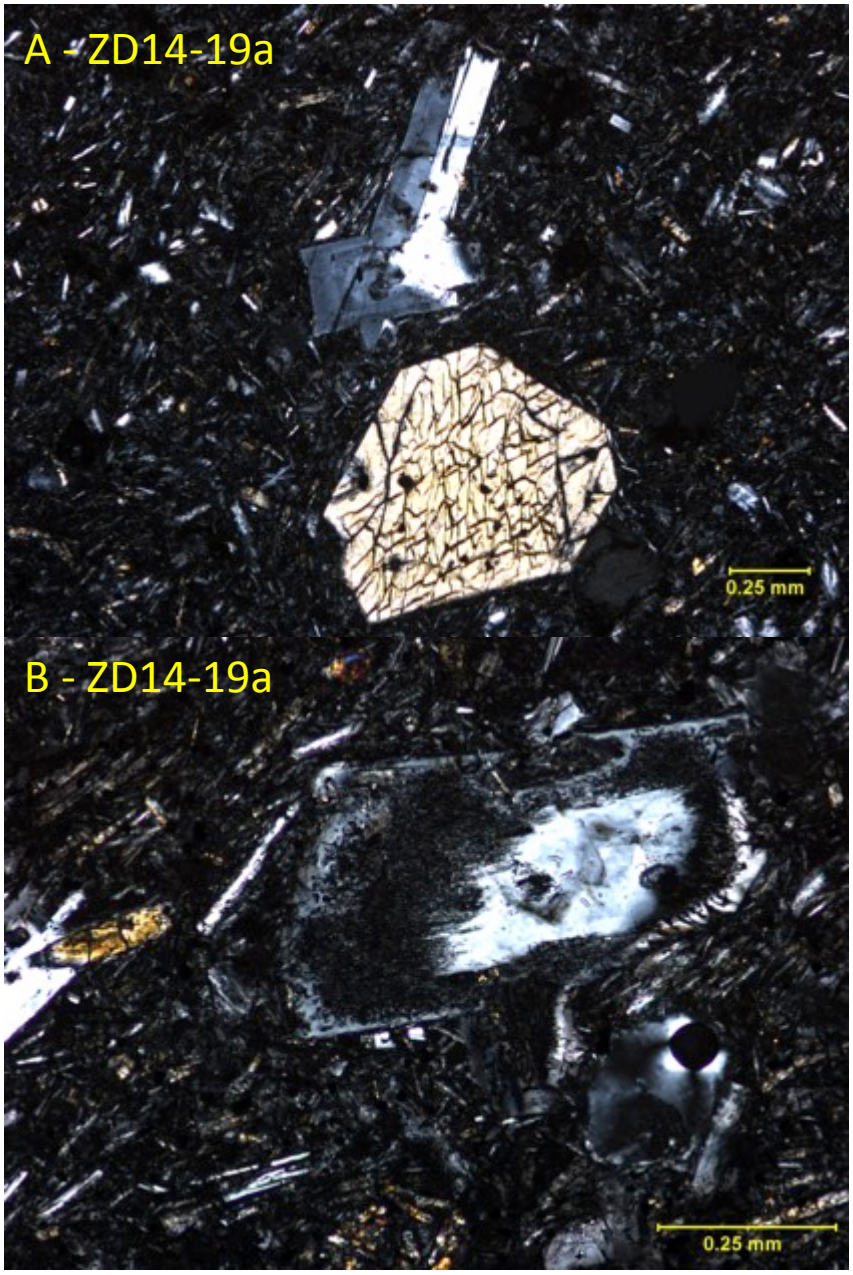

Figure 3-4 Wildcat Hill thin section photomicrographs

Photomicrographs of ZD14-19a displaying the fine-grained plagioclase dominated groundmass. (A) 4x magnification image. Clinopyroxene and plagioclase phenocrysts. (B) 10x magnification image. Plagioclase crystal exhibiting sieve texture.

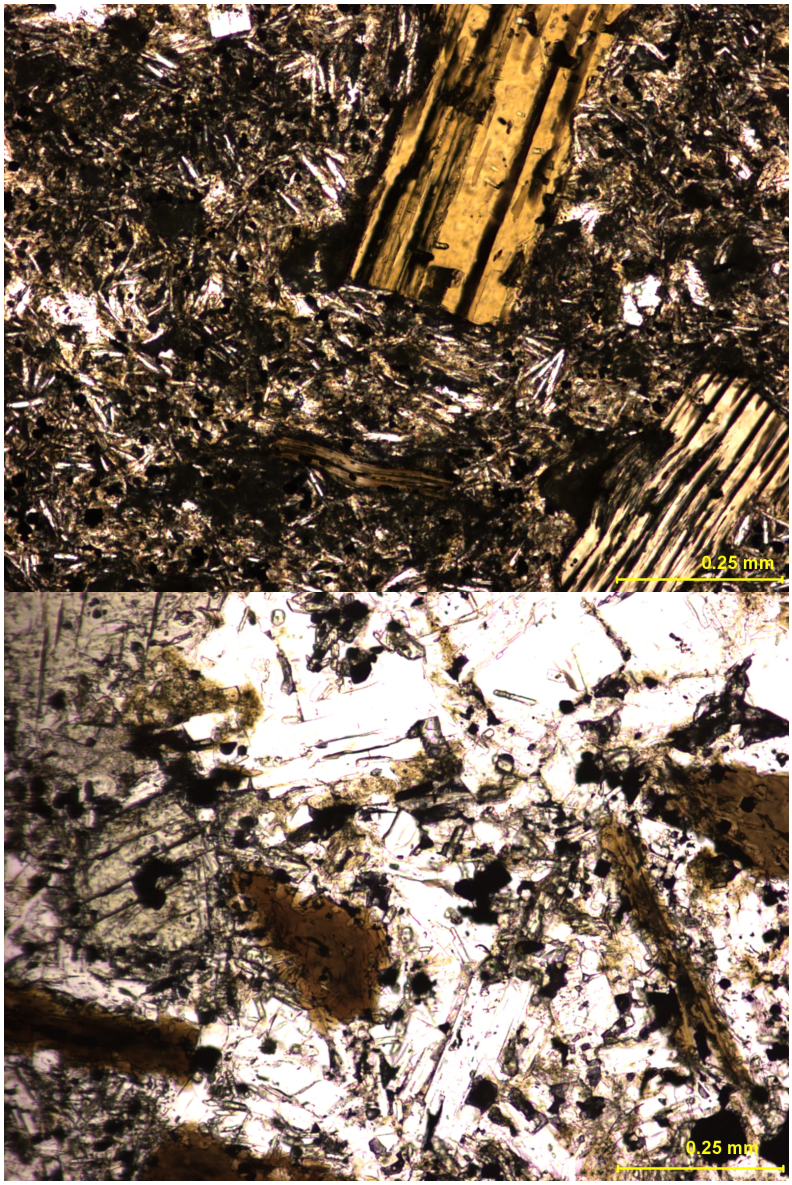

Figure 3-5 Textural differences between ZD14-5 and ZD14-6

Textural difference between ZD14-5 (top) and ZD14-6 (bottom) showing a glomerocryst of plagioclase, clinopyroxene, and mica. Both samples are from Pilot Knob, but exhibit significantly different groundmass textural sizes likely caused by varying temperatures during formation.

Light-coloured constituents		Predominant mafic minerals		
feldspar	foid	biotite > hornblende, ±diopsidic augite, (±olivine)	hornblende, diopsidic augite, ±olivine	brown amphibole, Ti-augite, olivine, biotite
or > pl	–	minette	vogesite	–
pl > or	–	kersantite	spessartite	–
or > pl	feld > foid	–	–	sannaite
pl > or	feld > foid	–	–	camptonite
–	glass or foid	–	–	monchiquite

Figure 3-6 Classification and nomenclature of lamprophyres based on their mineralogy (Le Maitre, 2002)

or = alkali feldspar; pl = plagioclase; feld = feldspar; foid = feldspathoid.

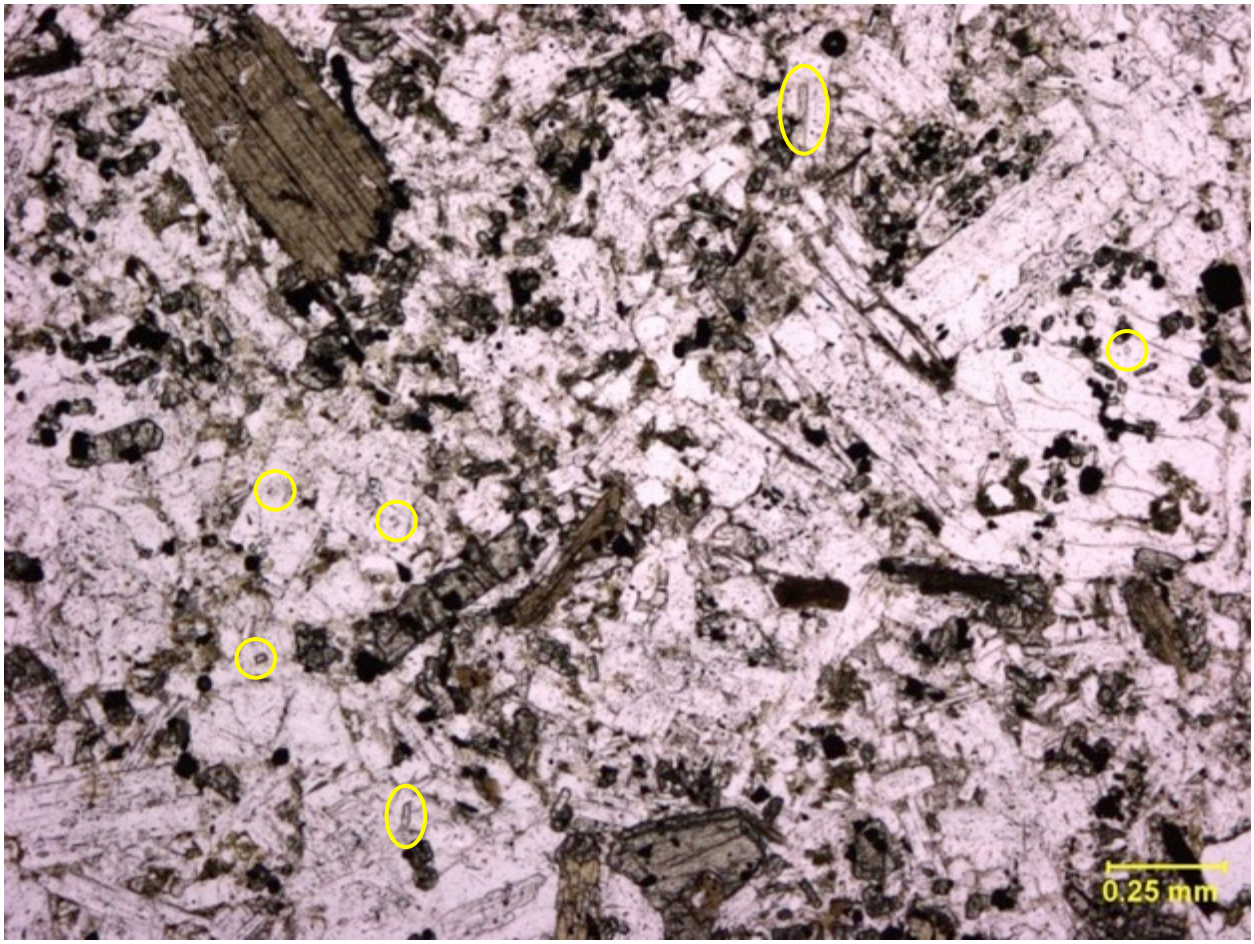

Figure 3-7 PPL thin section image of ZD14-5 with apatite

PPL image of ZD14-5 showing apatite crystals (circled in yellow) within the plagioclase dominated groundmass phase.

3.3 Bulk Geochemistry

Bulk major and trace element results are provided in Table 3-1.. Wildcat Hill and Pilot Knob appear to have fundamentally different geochemical compositions. All ICP-OES major and trace element data are reported on a volatile-free basis. Pilot Knob was found to be transitionally alkaline with SiO_2 values ranging from 54.48 to 55.30 wt. %; Wildcat Hill contains 63.27 to 63.62 wt. % SiO_2 and is subalkaline (Figure 3-5). On the total alkalis vs. silica diagram (Le Bas et al., 1986; Figure 3-6), Pilot Knob plots as basaltic trachyandesite and Wildcat Hill plots as dacite.

Major element bulk geochemistry indicated very little variation among Pilot Knob samples. Likewise, the two samples analyzed from Wildcat Hill showed little variations between each other. However, there are significant geochemical differences between Pilot Knob and Wildcat Hill. Harker diagrams were used to plot major elements (wt. %) versus SiO_2 (wt. %) (Figure 3-7). Pilot Knob rocks have higher concentrations of MgO, FeO*, K_2O, and P_2O_5 compared to Wildcat Hill, but lower Na_2O. Additionally, Pilot Knob and Wildcat Hill had relatively similar concentrations of CaO, Al_2O_3, and TiO_2.

For Pilot Knob, Al_2O_3 ranges from 15.6 to 17.0 wt. %, MgO ranges from 5.4 to 7.5 wt. %, CaO ranges from 7.7 to 7.9 wt. %, FeO* ranges from 5.5 to 5.7 wt. %, K_2O ranges from 3.7 to 4.1 wt. %, TiO_2 averages 0.9 wt. %, P_2O_5 ranges from 0.59 to 0.61 wt. %, and MnO ranges from 0.09 t 0.1 wt. %. Major element oxides for Pilot Knob samples show no apparent trends relative to SiO_2.

For Wildcat Hill, Al_2O_3 ranges from 16.08 to 16.09 wt. %, MgO ranges from 3.08 to 3.17 wt. %, CaO ranges from 5.1 to 5.12 wt. %, FeO* ranges from 4.74 to 4.78 wt. %, K_2O ranges from 2.28 to 2.45 wt. %, TiO_2 ranges from 0.69 to 0.7 wt. %, P_2O_5 averages 0.2 wt. %, and MnO averages 0.07 wt. %. As with Pilot Knob, the compositions of the two Wildcat Hill samples ae similar to one another..

Trace element bulk geochemistry also indicated little variation within the suite of Pilot Knob samples or between the two Wildcat Hill samples; however, Wildcat Hill and Pilot Knob remain consistently different from one another. Harker diagrams (Figure 3-8) were used to plot trace element data (ppm) versus SiO_2 (wt. %). Pilot Knob samples show higher concentrations of Ni, Cr, Ba, Sr, Zr, La, and Ce compared to Wildcat Hill. However, Wildcat Hill samples have higher concentrations of Nb.

Pilot Knob contained an average of 141 ppm Ni, 201 ppm Cr, 2,660 ppm Ba, 2,096 ppm Sr, 287 ppm Zr, 177.7 ppm La, 338.1 ppm Ce, and 7.8 ppm Nb. Wildcat Hill averaged 62 ppm Ni, 88 ppm Cr, 1,258 ppm Ba, 600 ppm Sr, 168 ppm Zr, 52.5 ppm La, 99.4 ppm Ce, and 9.3 ppm Nb.

Unlike Wildcat Hill, Pilot Knob showed light rare earth element (LREE) enrichment (Figure 3-9). When plotted on a chondrite-normalized REE diagram (Figure 3-11), the patterns exhibit a negative slope, with LREE enriched relative to HREE. Pilot knob contains 177 to 178 ppm La, 337 to 339 ppm Ce, 37.5 to 37.7 ppm Pr, 149 to 150 ppm Nd, 18.4 to 18.5 pp Sm, 3.75 to 3.76 ppm Eu, 4.6 to 4.71 pp Dy, 1.56 to 2.05 ppm Ho, and 1.31 to 1.53 ppm Yb. Wildcat Hill contains 52.3 to 52.7 ppm La, 98.9 to 99.0 ppm Ce, 12.1 to 12.8 ppm Pr, 39.8 to 40.0 ppm Nd, 6.84 to 7.01 pp Sm, 1.39 to 1.43 ppm, Eu, 3.32 to 3.4 pp Dy, 1.72 to 1.75 ppm Ho, and 1.16 to 1.17 ppm Yb.

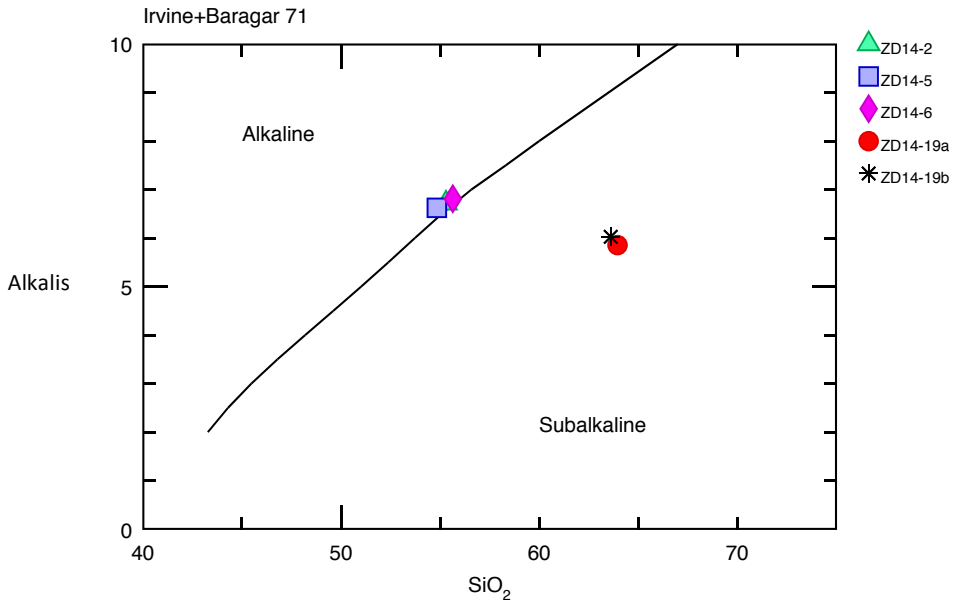

Figure 3-5 Alkaline vs. sub-alkaline XY diagram
Alkalis vs. wt.% SiO_2 plot showing Pilot Knob as transitionally alkaline and Wildcat Hill as subalkaline.

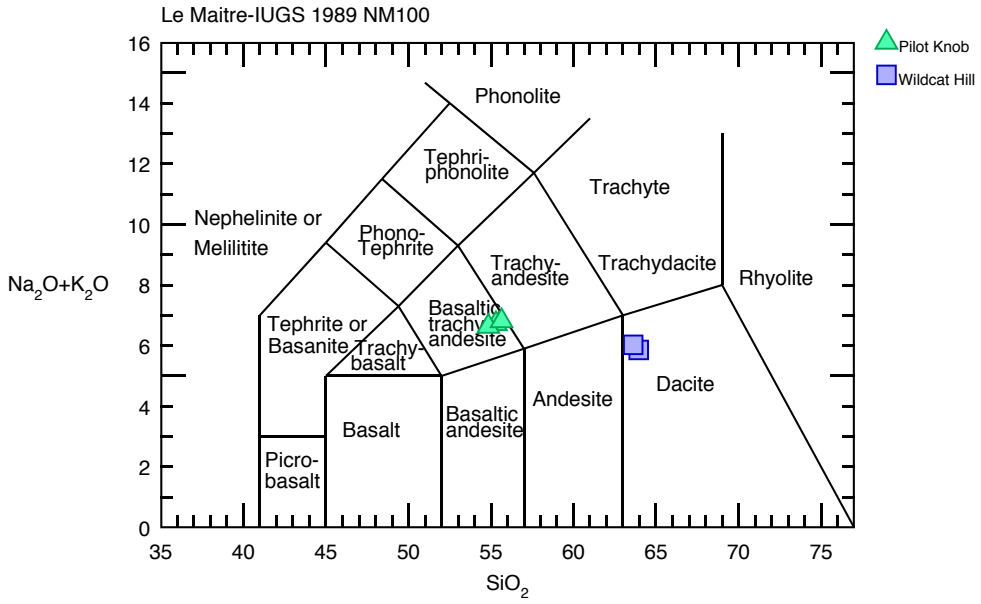

Figure 3-8 Total alkalis vs. silica diagram showing the difference in composition between Pilot Knob and Wildcat Hill (LeBas et al., 1986)

Rock classification diagram using major element concentrations. Pilot Knob samples plot as basaltic trachyandesite and Wildcat Hill samples plot as dacite.

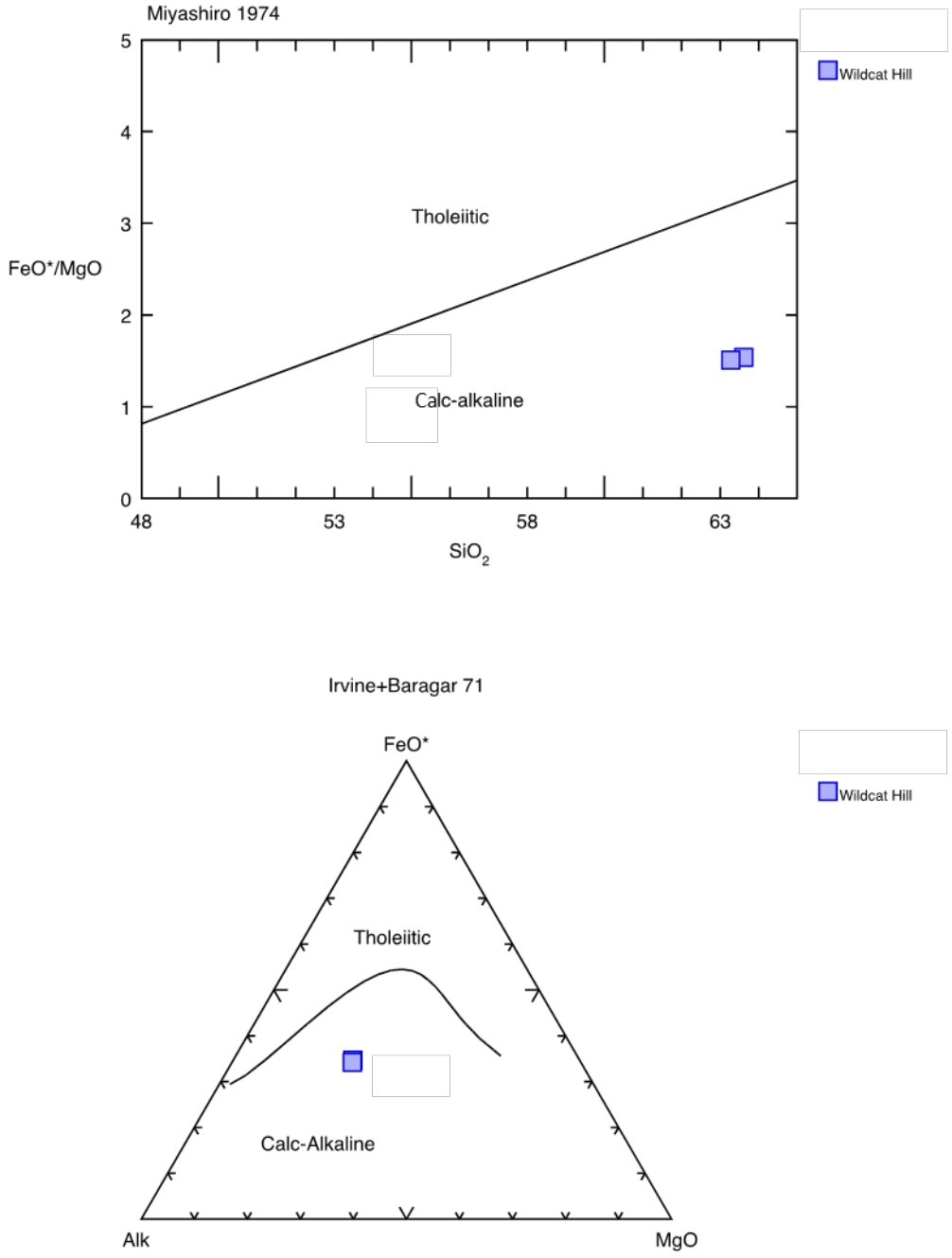

Figure 3-9 Discrimination diagram (Miyrashiro, 1974) and AFM diagram (Irvine and Baragar, 1971) used to distinguish between tholeiitic and calc-alkaline magmas.

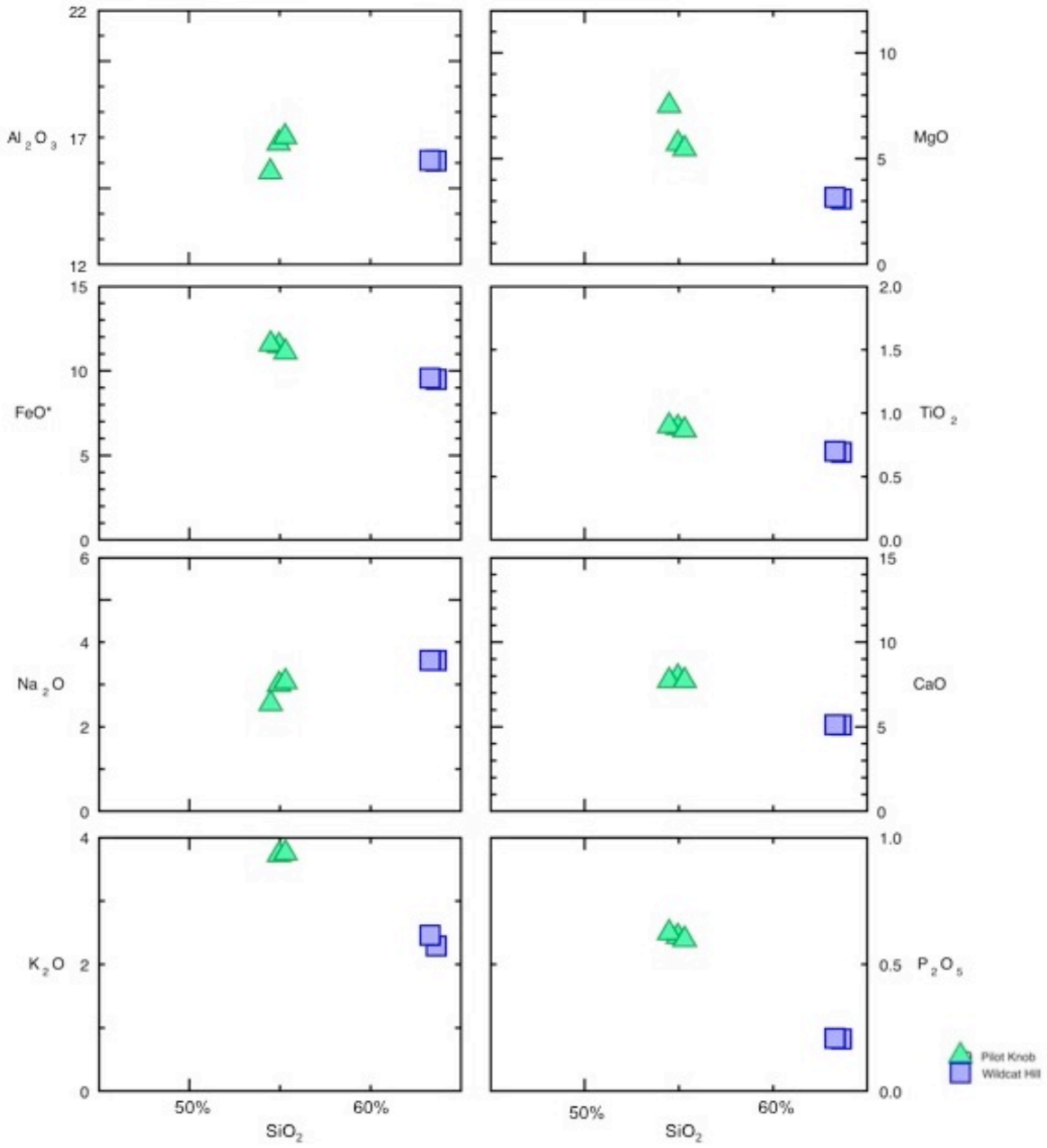

Figure 3-10 Harker diagrams showing major element concentrations in wt. %

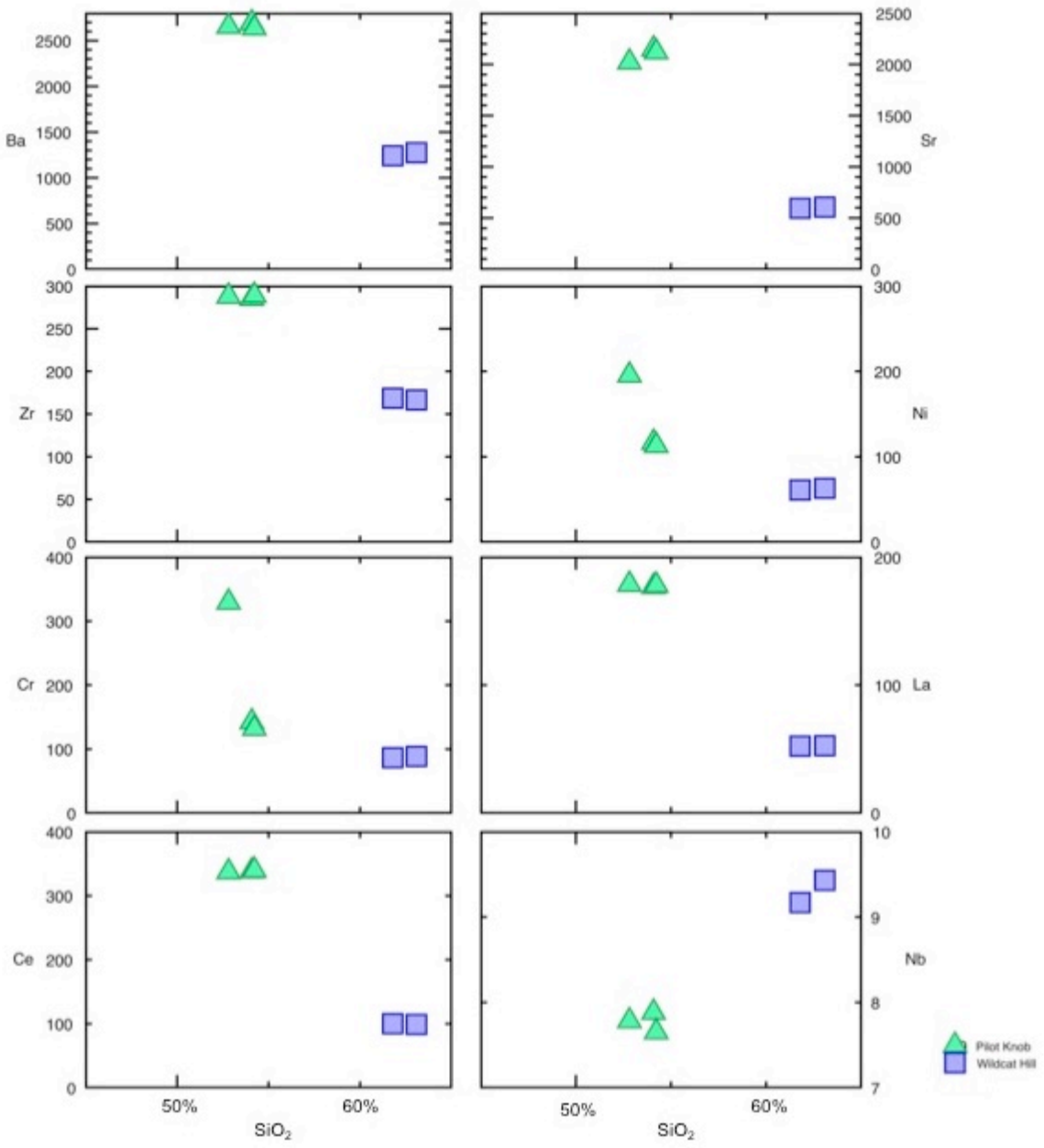

Figure 3-11 Harker diagrams showing concentrations of trace elements in ppm vs. wt. % SiO_2

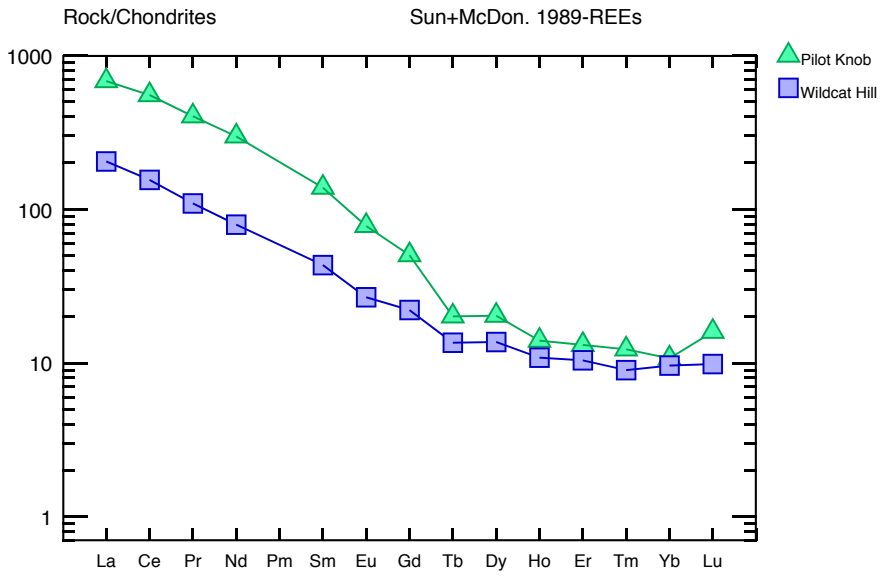

Figure 3-12 Chondrite-normalized REE plot diagram showing Pilot Knob and Wildcat Hill REE data.

Table 3-1 Bulk major and trace geochemistry data and isotope data for Pilot Knob (PK) and Wildcat Hill (WH)

Sample	**ZD14-2**	**ZD14-5**	**ZD14-6**	**ZD14-19A**	**ZD14-19B**
Location	Pilot Knob	Pilot Knob	Pilot Knob	Wildcat Hill	Wildcat Hill
SiO2	54.08	52.81	54.22	63.08	61.79
TiO2	0.87	0.87	0.85	0.69	0.68
Al2O3	16.50	15.15	16.69	15.95	15.72
Fe2O3	6.27	6.23	6.04	5.23	5.19
FeO	-	-	-	-	-
MnO	0.09	0.09	0.09	0.07	0.07
MgO	5.61	7.27	5.34	3.06	3.10
CaO	7.80	7.47	7.56	5.07	5.00
Na2O	2.95	2.46	3.00	3.54	3.49
K2O	3.66	3.96	3.68	2.27	2.40
P2O5	0.60	0.60	0.59	0.20	0.20
LOI	0.33	1.14	0.47	0.45	1.89
Total	98.75	98.07	98.51	99.61	99.55
Ni	117	195	113	63	61
Cr	142	329	132	88	86
Sc	15	15	14	11	11
V	127	118	123	86	88
Ba	2690	2654	2635	1274	1241
Rb	45	45	46	43	41
Sr	2147	2021	2119	606	595
Zr	285	288	289	167	169
Y	20	19	20	17	17
Nb	7.9	7.8	7.7	9.4	9.2
Cu	34	44	29	28	18
Co	28	32	28	16	18
Zn	73	82	80	66	77
Pb	33	36	33	22	23
La	176.8	178.5	177.8	52.7	52.3
Ce	338.2	336.8	339.3	98.9	100.0
Pr	37.5	37.6	37.7	12.8	12.1
Nd	150.3	150.1	148.9	39.8	40.0
Sm	18.5	18.5	18.4	7.01	6.84
Eu	3.75	3.75	3.76	1.43	1.39
Dy	4.67	4.6	4.71	3.4	3.32
Er	1.56	1.66	2.05	1.75	1.72

Yb	1.53	1.31	1.49	1.17	1.16
Be	2.34	2.52	2.35	1.44	1.42
Eu	3.75	3.75	3.76	1.43	1.39
Mo	5.92	1.01	5.39	6.74	6.37
$^{87}Sr/^{86}Sr$	0.70561	-	-	-	-
$^{144}Nd/^{143}Nd$	0.51151	-	-	-	-
$\varepsilon Nd_{3.5}$	-21.9	-	-	-	-

3.4 Mineral Chemistry

Electron Microprobe (EMP) data provided many mineralogical and elemental constraints for Pilot Knob and Wildcat Hill. Pyroxene, feldspar, mica, and apatite crystals were analyzed where available and general elemental compositions as well as specific REE data were compiled. Apatite data are listed in Table 1, biotite data is listed in table 5, feldspar data is listed in table 6, and pyroxene data is listed in table 7. Formulas used for recalculations and additional raw data are listed in Appendix C.

Pilot Knob feldspar crystals are transitional andesine to labradorite (Figure 3-8) with an average of 50.57 wt. % SiO_2, 30.87 wt. % Al_2O_3, 12.87 wt. % CaO, 3.44 wt. % Na_2O, 0.77 wt. % FeO, 0.45 wt. % K_2O, 0.10 wt. % MgO, and 0.01 wt. % MnO. Some weathering affecting the rim of the crystals was noted during petrographic analysis and rim/core points were analyzed to determine the effect of alteration; no measurable chemical difference was detected. Pyroxene crystals are diopside to augite (Figure 3-7) and average 50.66 wt. % SiO_2, 21.58 wt. % CaO, 15.60 wt. % MgO, 5.38 wt. % FeO, 4.19 wt. % Al_2O_3, 0.48 wt. % TiO_2, 0.31 wt. % Na_2O, .17 wt. % Cr_2O_3, 0.12 wt. % MnO, and 0.01 wt. % K_2O. The mica analyzed in Pilot Knob is primarily phlogopite (Figure 3-9) and averages 37.0 wt. % SiO_2, 18.98 wt. % MgO, 15.47 wt. % Al_2O_3, 9.0 wt. % K_2O, 8.85 wt. % FeO, 3.69 wt. % TiO_2, 2.82 wt. % H_2O, 1.93 wt. % F, 1.51 wt. % OH, 0.63 wt. % Na_2O, 0.07 wt. % MnO, and 0.02 wt. % CaO.

The mineral compositions in the Wildcat Hill rocks are geochemically distinct from those at Pilot Knob. Feldspars analyzed plotted as andesine and averaged 53.66 wt. % SiO_2, 29.41 wt. % Al_2O_3, 11.40 wt. % CaO, 4.68 wt. % Na_2O, 0.50 wt. % FeO, 0.22 wt. % K_2O, 0.06 wt. % MgO, and 0.01 wt. % MnO.

In addition to major mineral chemistry, the electron microprobe also proved useful for analyzing the apatite composition in sample ZD14-6 from Pilot Knob. Three points were analyzed. Trace element analysis for this sample indicated elevated LREE content. Data and specific parameters used are listed in Table 1.

Table 3-2 Electron Microprobe apatite crystal data. All data is displayed as wt. %.

Apatite	ZD14-5 AP1	ZD14-5 AP2	ZD14-5 AP3		ZD14-5 AP1	ZD14-5 AP2	ZD14-5 AP3
keV	25	25	25		25	25	25
Beam	5	10	10		5	10	10
Si	0.29	0.32	0.26	SiO2	0.62	0.68	0.56
Ti	< 0.021	< 0.022	< 0.023	TiO2	< 0.035	< 0.036	< 0.038
Th	< 0.046	< 0.046	< 0.032	ThO2	< 0.052	< 0.052	< 0.036
U	< 0.029	< 0.029	< 0.030	UO2	< 0.032	< 0.032	< 0.034
Al	< 0.008	< 0.007	< 0.008	Al2O3	< 0.015	< 0.013	< 0.015
Y	< 0.047	< 0.043	< 0.044	Y2O3	< 0.059	< 0.054	< 0.055
La	< 0.067	0.11	0.15	La2O3	< 0.078	0.13	0.18
Ce	0.20	0.27	0.21	Ce2O3	0.23	0.32	0.25
Pr	< 0.082	< 0.077	< 0.076	Pr2O3	< 0.095	< 0.090	< 0.088
Nd	0.10	0.13	0.09	Nd2O3	0.12	0.15	0.10
Sm	< 0.069	< 0.071	< 0.072	Sm2O3	< 0.080	< 0.082	< 0.083
Eu	< 0.064	< 0.069	< 0.070	Eu2O3	< 0.074	< 0.079	< 0.081
Gd	< 0.066	< 0.066	< 0.069	Gd2O3	< 0.076	< 0.076	< 0.079
Tb	< 0.038	< 0.039	< 0.039	Tb2O3	< 0.043	< 0.044	< 0.044
Dy	< 0.037	0.04	0.04	Dy2O3	< 0.042	0.05	0.05
Ho	< 0.052	< 0.054	< 0.053	Ho2O3	< 0.059	< 0.061	< 0.060
Er	< 0.035	< 0.037	< 0.039	Er2O3	< 0.040	< 0.042	< 0.044
Tm	< 0.035	0.04	< 0.037	Tm2O3	< 0.039	0.05	< 0.042
Yb	< 0.035	< 0.036	< 0.034	Yb2O3	< 0.039	< 0.040	< 0.038
Lu	< 0.027	< 0.029	< 0.028	Lu2O3	< 0.030	< 0.032	< 0.031
Fe2+	0.21	0.27	0.19	FeO	0.27	0.35	0.24
Mn2+	0.03	0.04	0.02	MnO	0.04	0.05	0.03
Mg	0.25	0.26	0.25	MgO	0.41	0.43	0.41
Ca	37.94	37.87	38.20	CaO	53.09	52.99	53.45
Sr	0.40	0.37	0.44	SrO	0.47	0.44	0.52
Ba	< 0.043	< 0.039	< 0.041	BaO	< 0.048	< 0.043	< 0.045
Na	0.13	0.15	0.15	Na2O	0.18	0.20	0.20
P	15.39	16.79	17.08	P2O5	35.26	38.47	39.14
S	0.35	0.38	0.36	SO3	0.87	0.95	0.90
F	5.73	5.20	4.74				
O	36.42	38.33	38.71	F	5.73	5.20	4.74
O=anion	-2.41	-2.19	-2.00	O=anion	-2.41	-2.19	-2.00
Total	95.03	98.36	98.92	Total	94.88	98.26	98.76

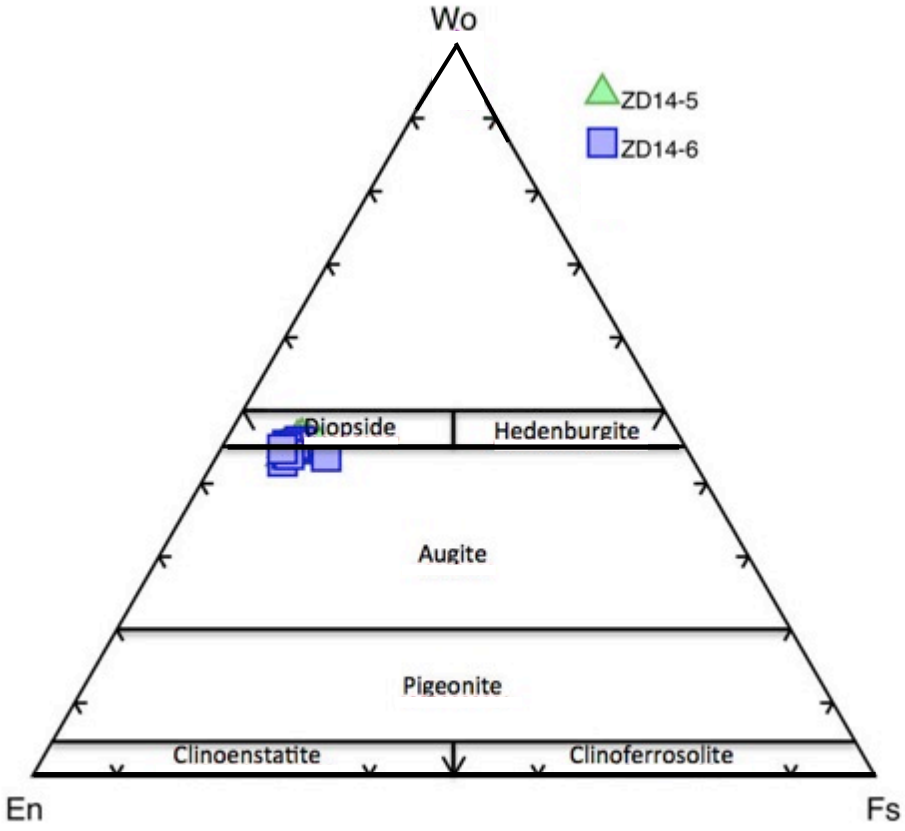

Figure 3-13 Pyroxene ternary diagram

Ternary diagram showing pyroxene endmember and classifications. Pilot Knob is transitionally augite – diopside.

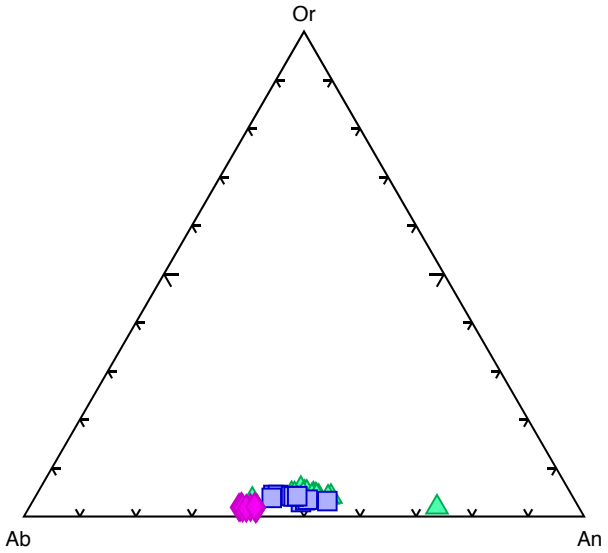

Figure 3-14 Feldspar ternary diagram

Feldspar ternary diagram showing Wildcat Hill is primarily andesine and Pilot Knob is transitionally andesine to labradorite.

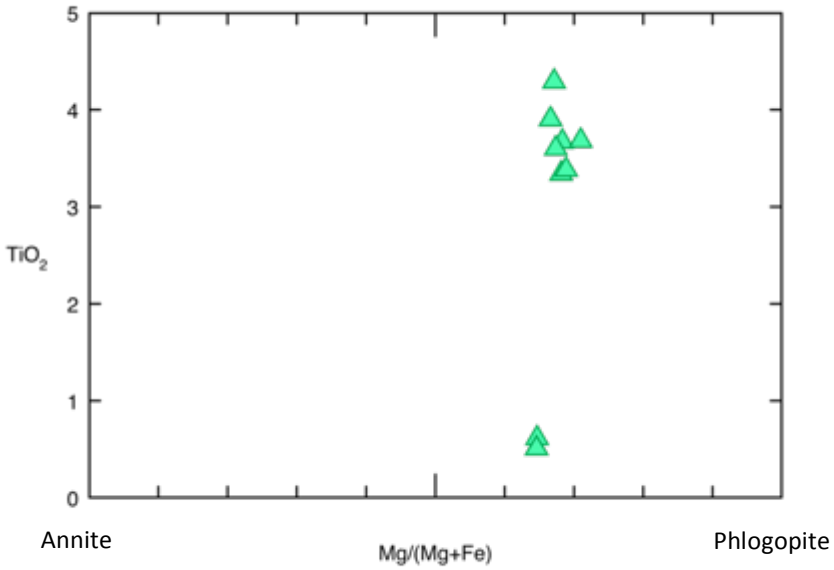

Figure 3-15 TiO_2 vs. Mg/(Mg+Fe) plot - mica compositions

Diagram showing annite vs. phlogopite compositions. All points are from sample ZD14-6 and plot as phlogopite.

3.5 Isotope geology

One sample, ZD14-2, was selected for new Sm/Nd isotope data to help determine petrogenetic constraints and decipher the origin of Pilot Knob. The measured $^{143}Nd/^{144}Nd$ ratio is 0.51151 ± 0.000012. Epsilon Nd at t=3.5 Ma was calculated as -21.9. The Leucite Hills lamproites, which have been found to indicate an ancient Wyoming craton lithospheric mantle source that has undergone varying degrees of enrichment and depletion, have $^{143}Nd/^{144}Nd$ values ranging from 0.51178 – 0.51211 and εNd values for the phlogopitic lamproites ranging from -13.5 to -15(Mirnejad and Bell, 2006). Pilot Knob isotopic values correlate closely to those of the Leucite Hills lamproites, further indicating a similarity (Downey, 2015; this study). Locally, Spring Mountain basalts have εNd = -18.3, Crescent Mountain basalt measures -22.2, and Lava Mountain samples range from -19.5 to -22.2 (Downey, 2015). Lithospheric mantle has a radiogenic εNd isotope composition of <<0 which is similar to all analyzed samples in the UWRB. Furthermore, these Nd isotope results coupled with Sr-Pb data from Pilot Knob, Spring Mountain, and Crescent Mountain together indicate an affinity to ancient lithospheric mantle (Downey, 2015)..

3.6 Thermobarometry

All pyroxene crystals from Pilot Knob plotted as primarily diopside (clinopyroxene). According to extensive work by Putirka (2008), clinopyroxene compositions can be used as geobarometers and geothermometers to help reconstruct temperature and depth of crystallization. Over the last several decades, there have been many geobarometer models developed to encompass a vast range of igneous compositions and environments. When limited data exist covering a specific area of interest, such models can provide useful information on the conditions that may have existed during petrogenesis. All geothermobarometry results were found using Putirka's (2008) equations listed for using clinopyroxene vs. bulk geochemistry. Bulk geochemistry and electron microprobe data were input into a spreadsheet provided by Putrika, 2008 and final data are listed in Figure 3-9; a full list of geobarometers and geothermometers created by Putrika can be found here: http://www.fresnostate.edu/csm/ees/faculty-staff/putirka.html. Clinopyroxene data, upon first observation, indicate that crystallization of clinopyroxene (and thus potentially the Pilot Knob intrusive body) did not occur in the shallow crust. However, field-relationships (e.g., Pilot Knob intruding non-metamorphosed Eocene

volcaniclastic strata derived) indicate that Pilot Knob had to have intruded the Eocene strata in the upper crust, at fairly shallow depths. Thus, the data suggests that clinopyroxene from Pilot Knob appears to have last equilibrated at greater depths. Assuming a lithostatic gradient average of 3.3km/1kbar (Raymond, 2007), an average depth of crystallization can be calculated. ZD14-5 averaged 7.2 kilobars indicating a depth of 23.8 km; ZD14-6 averaged 4.2 kilobars indicating a depth of 13.86 km. Textural differences were also noted between these two samples (Figure 3-5).

Table 3-3 Geothermometer and geobarometer data for ZD14-5 and ZD14-6 clinopyroxene crystals (Putrika, 2003)

Temperature and pressure data indicate clinopyroxene crystallization at mid-crustal levels (~21 km depth).

	Temperature (Degrees C)	Pressure (Killobars)	Depth (Km)
ZD14-5	1182.3	6.8	22.6
	1196.6	8.4	27.6
	1190.4	7.7	25.3
	1194.2	8.0	26.5
	1197.7	8.4	27.7
	1196.9	8.4	27.7
	1182.2	6.7	22.1
	1192.8	7.8	25.6
	1187.5	7.3	24.1
	1199.7	8.7	28.6
	1191.5	7.8	25.8
	1195.6	8.0	26.4
Average	1187.5	7.2	**23.9**
ZD14-6	1145.1	4.3	14.2
	1146.4	4.5	14.7
	1143.5	4.1	13.7
	1148.0	4.6	15.3
	1132.9	2.7	8.9
	1147.1	4.5	14.8
	1144.6	4.2	14.0
	1129.6	2.5	8.1
	1158.0	5.6	18.4
	1141.2	3.9	13.0
	1161.3	5.7	18.7
Average	1145.3	4.2	**14.0**

Chapter 4 - DISCUSSION

The Quaternary magmatic event(s) that gave rise to Pilot Knob and Wildcat Hill are only poorly recognized beyond local UWRB studies (e.g.: Keefer, 1970; Love, 1960; Blackstone, 1993; Adams, 2014; Downey et al., 2014). Thus, this work represents an important new source of data for understanding the cause of young UWRB magmatism as well as possible links to other regional alkaline rocks. Furthermore, this work provides new data on rare earth element occurrence in alkaline igneous complexes within the UWRB, furthering U.S. exploration potential for the REEs.

Both field and laboratory research were used to search for any similarities with the surrounding regional geology. Regionally, Pilot Knob and Wildcat Hill could be related to Yellowstone volcanism, the Leucite Hills in southwest WY, and/or Basin and Range extension correlating to the Upper Wind River Basin region. Structural characteristics, geochemical constraints, and age dates were all considered.

4.2 Regional structure

Extensive geologic mapping outlining faulting and regional structures have been published covering the proximity of YSNP and the Eastern Snake River Plane (ESRP), there are also structure maps documenting faults and structure throughout Wyoming. Initial study of satellite imagery and topographic maps indicates multiple igneous intrusive complexes that all trend northwest-southeast (Figure 1-6). Upon further investigation, these igneous intrusions appeared to be shallow features, indicative of dikes that reached the surface. This remains consistent with the initial observation that these hypothesized shallow intrusives all trend between 300 and 330 degrees. This observation indicates that regionally extensive faults likely acted as conduits for these intrusive bodies.

Using geochemical constraints and regional observations, it appears that although geochemically different, the shallow intrusive complexes present in the Upper Wind River Basin region may still be structurally related. It is theorized that the north-south normal faulting observed is a structural feature that has extended south through the study area from YSNP (Figure 3-1) which could be related to basin-range development in the UWRB. A well-documented example of this is the Teton normal fault, which formed the Teton range and has

been active in recent history (Byrd, et al., 1994). Based on these observations, it is reasonable to hypothesize that UWRB magmas have exploited the aforementioned structural fabric in northwest Wyoming, which could explain how the numerous relatively small intrusions have migrated to the surface.

4.3 REE Potential

Apatite is an important REE-bearing mineral and can explain the elevated occurrences of LREE's in Pilot Knob geochemistry, because it can contain relatively high concentrations of REEs (most commonly Ce and La) (Fig. 2-2). As outlined in the electron microprobe section of this chapter, the apatite crystals found included in plagioclase exhibit elevated concentrations of Ce, La, and Nd. These high occurrences of REEs in apatite are presumably what caused the bulk geochemistry from the ICP-OES analysis to read 200-300 ppm for these elements.

ICP-OES data show elevated Ce, La, and Nd concentrations (~600 ppm) in the Pilot Knob samples, but not in Wildcat Hill (< 200 ppm). Pilot Knob samples showed homogeneity with trace element analysis as well. As seen in Figure 4-1, bulk geochemistry shows Pilot Knob samples contain ~338 ppm Ce, ~176 ppm Nd, and ~149 ppm Nd. This corresponds to a total ore lode of approximately 665 ppm LREE (0.065 wt. %). When compared to other REE deposits around the world, Pilot Knob does not appear to be of significant economic potential currently. Bayan Obo for example, the world's largest REE producer, produces approximately 0.13 wt. % Nb and has an average REO grade of 6 wt. % (Zhi Li & Yang, 2014). Additionally, Mountain Pass, California contains >5 wt. % REO's (Olson, et al., 1954). With this taken into consideration, Pilot Knob does not posess any current REE economic potential, however as technology progresses and new means of extracting REOs are developed, Pilot Knob and similar deposits may become viable. Additionally, during petrographic analysis, apatite was identified as a groundmass phase mineral in all Pilot Knob samples, where it occurred intergrown with plagioclase (Figure 4-2). Apatite has been found to be a primary REE-bearing mineral in alkaline intrusive rocks (Lingdi and Yangchuan, 1989). Apatite has also been recognized as a potential petrogenetic tracer because of the wide variations in major and trace element abundances in accordance with the magma it formed in (Chu et al., 2009). For the purpose of this study, it was found to be the host mineral for the elevated REEs. No other potential REE-bearing minerals were identified in the Pilot Knob samples. It is important to note however, that the three primary

commercially exploited REE-bearing minerals are bastnasite, monazite, and xenotime (Jordens, et al., 2013), not apatite.

The apatite observed in Pilot Knob samples, as outlined in the petrography results section, is small (generally <0.1 mm) and occurs as inclusions or intergrown with plagioclase. Data from three separate apatite crystals analyzed from sample ZD14-5 (Table 1) show significantly elevated Ce (23 wt. %), La (13 wt. %), and Nd (11 wt. %). Comparing these numbers with the bulk geochemistry data, it is evident that the elevated LREE concentrations are a result of the LREE-rich apatite within Pilot Knob. However, aside from a select few locations (e.g., the Kovdor Massif, Russia), apatite has exhibited little economic potential as a REE-bearing ore mineral (Jordens, et al., 2013). As technology continues to advance though, this may change. When compared to other REE deposits worldwide, although relatively low (0.065 wt. % REE), Pilot Knob certainly shows potential for future LREE exploration.

4.4 Petrogenesis

The most similar, young, alkaline igneous complex proximal to Pilot Knob is the Leucite Hills lamprophyre (LHL). Leucite Hills petrography data indicate that the samples consist primarily of phlogopite, diopside, sanidine, leucite, apatite, and other trace minerals (Mernejad and Bell, 2006). Of these, phlogopite, clinopyroxene, and apatite can occur as phenocrysts, similar to Pilot Knob (Mernejad and Bell, 2006). Figure 4-1 shows Pilot Knob and Wildcat Hill plotted along with data for Leucite Hills lamproites; both my study area and LHL data show enrichment of the LREE relative to the HREE, although the REE patterns for Leucite Hills are steeper with lower concentrations of the HREE. This suggests a greater role for garnet in the mantle source for the LHL lamproites than for Pilot Knob or Wildcat Hill. The flat HREE pattern both exhibit indicates HREEs are controlled by clinopyroxene, thus mantle melting of spinel peridotite likely occurred to generate the Pilot Knob magma.

Petrographic and textural data and field analysis indicate that Pilot Knob is a *shallow* intrusive complex. This can be justified by developing a complex or multi-stage developmental history. Presumably, the clinopyroxene crystals, along with the other larger phenocryst phase minerals formed in a magma body that resided at >20 km depth. The samples analyzed in ZD14-6 that yielded a pressure of 3.9 kb, corresponding to a depth of ~13 km, suggest that these clinopyroxene crystals formed as the magma continued to migrate upwards towards the Earth's

surface. This "slurry" was then forced upward to shallower depths where the melt began to cool more rapidly, forming the plagioclase dominated groundmass noted in all Pilot Knob thin sections. The textural differences noted between ZD14-5 and ZD14-6 are consistent with this hypothesis. This is also consistent with the Leucite Hills hypothesis of a multi-stage formation process (Mernejad and Bell, 2006).

The more recent magma melting that occurred to cause the formation of Pilot Knob and Wildcat Hill is potentially due to the Yellowstone Hotspot (Downey, 2015). The associated lithospheric thinning and mantle upwelling (plus thermal effects) related to the Yellowstone plume could have caused the melting and subsequent volcanism that formed the Cenozoic UWRB volcanics, Pilot Knob, and Wildcat Hill (Downey, 2015). Conversely, melting could have been generated via Basin and Range faulting, unrelated to the hotspot; more work is needed to fully decipher these relationships.

Pilot Knob and Wildcat Hill are not petrogenetically related. Pilot Knob is a basaltic trachyandesite that can also be considered a kersantite-type lamprophyre. In contrast, Wildcat Hill is a sub-alkaline dacite. However, Pilot Knob major and trace element chemistry correlate well with the Leucite Hills, as outlined by Mernejad and Bell (2006). Pilot Knob LREE data plot closely with the madupitic Leucite Hills data.

Nd isotope data also indicates a multistage magmatic history. With an $\varepsilon Nd_{3.5}$ value of -21.9, it is evident that Pilot Knob magmatism originated from an Archean lithospheric mantle source. Downey (2015) suggests that this is 2.8 Ga lithospheric mantle associated with the Wyoming craton (e.g., lithospheric mantle that reflects 2.8 Ga Beartooth stabilization age). These data, coupled with the 3.4 Ma K-Ar age date (Obradovich, 1978) and with other field and petrographic data, indicate Pilot Knob is a young, shallow intrusive complex with lithospheric mantle origins that has undergone a multi-stage/multi-depth crystallization history.

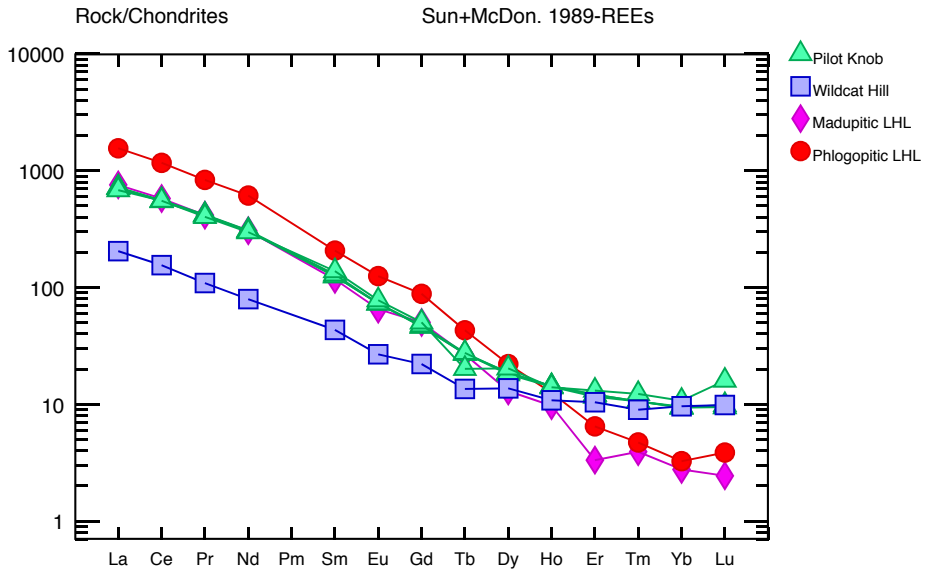

Figure 4-1 Chondrite-normalized REE diagram showing whole-rock data for Pilot Knob, Wildcat Hill, and Leucite Hills (phlogopitic and madupitic).

REE diagram showing Pilot Knob and Leucite Hills REE data (LHL data from Mirnejad & Bell, 2006).

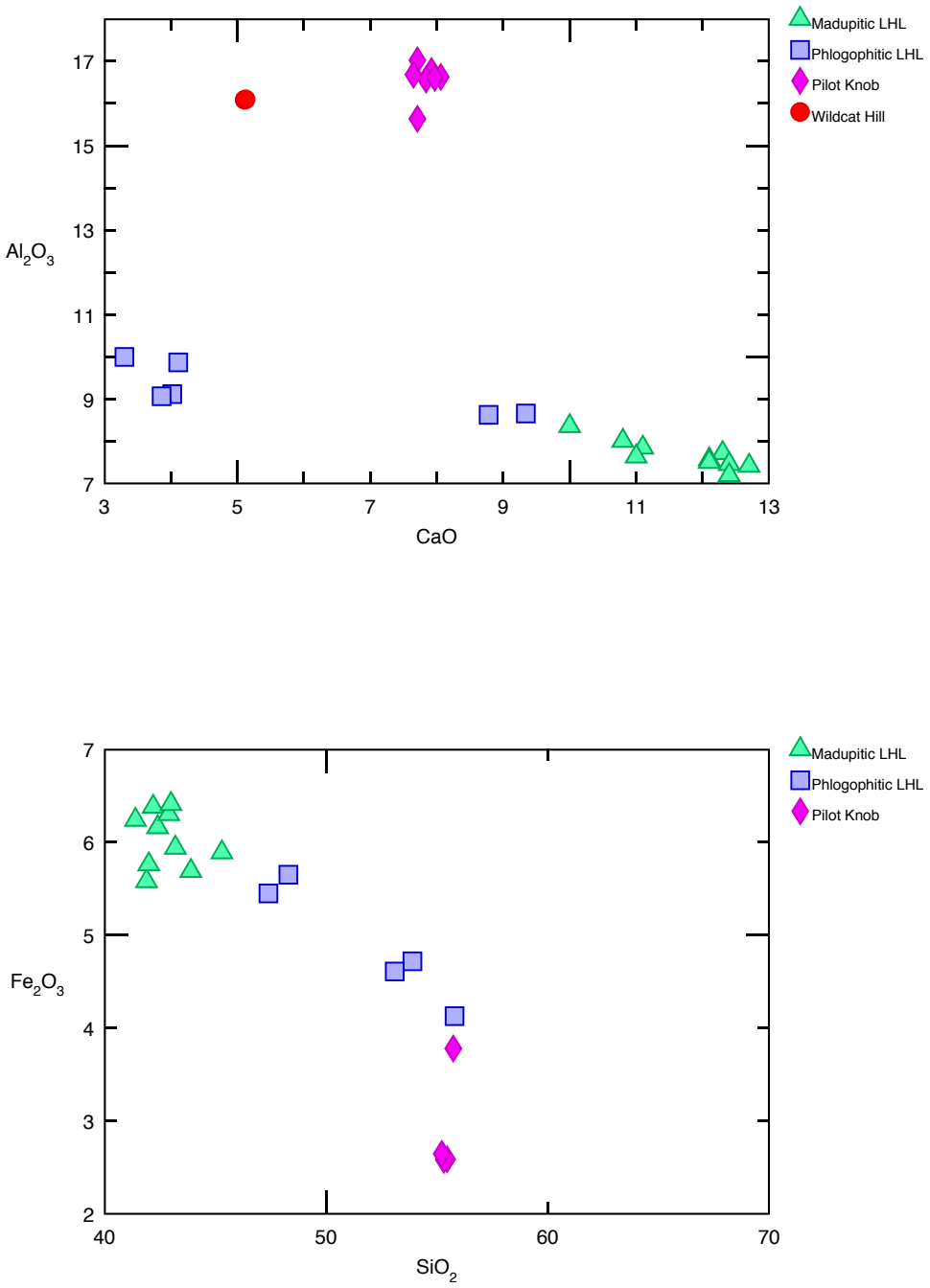

Figure 4-2 Fe_2O_3 vs. SiO_2 and Al_2O_3 vs. CaO diagrams with LHL data

Fe_2O_3 vs. SiO_2 diagram showing Pilot Knob plotted against madupitic and phlogopitic samples from the Leucite Hills (data adapted from Mirnejad & Bell, 2006)

Chapter 5 - SUMMARY

Using detailed field reconnaissance, petrography, and geochemistry, I have been able to make correlations with Pilot Knob and Wildcat Hill to the regional geology of northwest Wyoming, USA. First, Pilot Knob, Wildcat Hill, and other intrusive complexes in the UWRB region all trend northwest. Observing the extensive normal faulting and tectonism in the region (Figure 1-6), all of these complexes appear to be directly correlated to these faults, suggesting they are conduits through which magma was able to migrate towards the surface. The Yellowstone hotspot related lithospheric thinning and mantle upwelling is presumed to be the regional source of melting for these intrusions. Although Pilot Knob and Wildcat Hill exhibit few geochemical similarities, emplacement to the surface is presumably related to this faulting in both cases.

Pilot Knob Nd isotope data (coupled with Sr-Nd-Pb results from other upper Wind River Basin Cenozoic volcanics; Downey, 2015) indicate ancient lithospheric mantle origins and the other bulk chemical data and mineral chemistries, suggest a multi-stage development history and crystallization at varying depths. Textures and field observations indicate a shallow, near surface intrusion that then underwent significant glacial erosion in recent history, exposing much of the intrusion. Geobarometry and isotope data indicate mid-crust crystallization histories moving progressively shallower (ZD14-5 then ZD14-6). Finer-grained textural changes within the groundmass phase of Pilot Knob support this theory, indicating larger crystals forming at depth, then cooling accelerating as it progressed towards the surface.

Finally, Pilot Knob may contain economic LREE potential for the future. Although limited today by modern recovery and mining techniques, Pilot Knob and similar LREE-bearing alkaline igneous intrusive complexes within the United States have potential as economically viable REE deposits with the advancement of technology. Additionally, as the world continues to grow and expand, technology advancements will increase the demand for REEs and their corresponding technologies. Currently, the largest obstacle to make Pilot Knob economically viable is an efficient method with which to extract the LREE-bearing apatite in order to extract the Ce, La, and Nd. With an increased demand, new REE deposits will be explored and new processing techniques will be developed, making locations such as Pilot Knob of interest.

Furthermore, Pilot Knob's proximity to a major highway (U.S. Highway 287) and Wyoming's already thriving mining economy will contribute to the appeal of Pilot Knob as well.

References

Ander, M., Saltzman, J., and Hemming, S., 2009, Neogene tephra correlations in eastern Idaho and Wyoming: Implications for Yellowstone hotspot-related volcanism and tectonic activity, GSA Bulletin, Vol. 121, no. 5-6, pp. 837-856, doi: 10.1130/B26300.1

Blackstone, D. L., 1966, Pliocene volcanism, southern Absaroka Mountains, Wyoming, Rocky Mountain Geology, Vol. 5, pp. 21-30

Blackstone, D. L., 1993, The Wind River Range, Wyoming: An Overview, Jubilee Anniversary Field Conference Guidebook: Wyoming Geology, Past, Present, and Future, pp. 121-140

Byrd, J., Smith, R. B., Geissman, J. W., 1994, The Teton fault, Wyoming: Topographic signature, neotectonics, and mechanisms of deformation, Journal of Geophysical Research (99), No. B10, pp. 20095-20122

Castor, S. B., 2008, The Mountain Pass rare-earth carbonatite and associated ultrapotassic rocks, California, The Canadian Mineralogist, Vol. 46, p. 779-806, doi: 10.3749/cammin.46.4.779

Chachmouradian, A. R. and Wall, F., 2012, Rare Earth Elements: Minerals, Mines, Magnets (and More), Elements, Vol. 8, pp. 333-340.

Christiansen, R. L., Foulger, G.R., and Evans, John R., 2002, Upper-mantle origin of the Yellowstone hotspot, GSA Bulletin, Vol. 114, No. 10, p. 1245-1256

Christiansen, R. L. (2001) The Quaternary and Pliocene Yellowstone Plateau volcanic field of Wyoming, Idaho, and Montana [Geologic Map]. United States Geological Survey, Professional Paper 729-G.

Chu, M., Wang, K., Griffin, W. L., Chung, S., O'Reilly, S. Y., Pearson, N. J., and Jizuka Y., 2009, Apatite Composition: Tracing Petrogenetic Processes in Transhimalayan Granitoids, Journal of Petrology, Vol. 50, No. 10, pp. 1829-1855, doi: 10.1093/petrology/egp054

Cornel, D. H., 1993, Rare Earths from Supernova to Superconductor, Pure and Applied Chemistry, Vol. 65, No. 12, pp. 2453-2464

Deer, W. A., Howie, R. A., Zussman, J., 1996, The Rock-Forming Minerals, 2nd Edition, Logman Scientific & Technical, ISBN 0-582-30094-0

Dobranksy, S., 2013, Rare Earth Elements and U.S. Foreign Policy: The Critical Ascension of REEs in Global Politics and U.S. National Secutiry, American Diplomacy, Commentary and Analysis, October 2013, http://www.unc.edu/depts/diplomat/item/2013/0912/ca/dobransky_rareearth.html

Downey, A. C., 2015, Cenezoic Mafic to Intermediate Volcanism at Lava Mountain and Spring Mountain, Upper Wind River Basin, Wyoming, M.S. Thesis, Kansas State University, Manhattan, Kansas

Downey, A., Dodd, Z., Brueseke, M., and Adams, D., 2014, Geochemical constraints on Cenozoic intraplate magmatism in the Upper Wind River Basin, Wyoming (USA), American Geophysical Union, 2014 Fall Meeting, abstract #19607

Downey, A., Brueseke, M., Hart, W., 2014, New geochemical constraints on quaternary mafic volcanism in the Upper Wind River Basin, Wyoming (U.S.A), Geological Society of America *Abstracts with Programs.* Vol. 46, No. 5, p.82

Erslev, E. A., Koenig, N. V., 2009, Three-dimensional kinematics of Laramide, basement-involved deformation, USA: Insights from minor faults and GIS-enhanced structure maps, Geological Society of America Memoirs, Vol. 204, pp. 125-150, doi: 10.1130/2009.1204(06)

Fox, J. E., Dolton, G. L., 1995, Wind River Basin Province, USGS National Oil and Gas Assessment. http://certmapper.cr.usgs.gov/data/noga95/prov35/text/prov35.pdf

Gasching, R. M., Vervoort, J. D., Lewis, R. S., Tikoff, B., 2011, Isotopic Evolution of the Idaho Batholith and Challis Intrusive Province, Northern US Cordillera, Journal of Petrology, Vol. 52, pp. 2397-2429, doi: 10.1093/petrology/egr050

Housel, D. W., 2014, A Guide to Finding Gemstones, Gold, Minerals, & Rocks, CreateSpace Independent Publishing Platform, ISBN-10: 1502513889

Jordens, A., Cheng, Y.P., Waters, K.E., 2013, A review of the beneficiation of rare earth element bearing minerals, Minerals and Engineering, Vol. 41, pp. 97-114

Kanazawa, Y. and Masaharu, K., 2006, Rare earth minerals and resources in the world, Journal of Alloys and Compounds, Vols. 408-412, p. 1339-1343, doi:10.1016/j.jallcom.2005.04.033

Keefer, W.R., 1965, Geologic History of the Wind River Basin, Central Wyoming, AAPG Bulletin, Vol. 49, Issue 11, pp. 1872 – 1892

Keefer, W.R., 1970, Structural Geology of the Wind River Basin, Wyoming, Geological Survey Professional Paper 495-D

Kynicky, J., Smith, M. P., Xu, C., 2012, Diversity of rare earth deposits: the key example of China: Elements, 8, doi: 10.2113/gselements.8.5.361

Le Bas, M. J., Le Maitre, R. W., Streckeisen, A., Zanettin, B, 1986, A chemical Classification of volcanic rocks based on the total alkali-silica diagram, Journal of Petrology, Vol. 27, pp. 745-750

Le Bas, M. J. and Streckeisen, A. L., 1991, The IGUS systematics of igneous rocks, Journal of the Geological Society, London, Vol. 148, pp. 825-833

Le Maitre, R. W., Streckeisen, A. L., Zanettin, B., Le Bas, M. J., Bonin, B., and Bateman, P., 2002, Igneous Rocks: A Classification and Glossary of Terms, Cambridge, UK: Cambridge University Press, 236p.

Lingdi, Z., Yangchuan, W., 1989, REE geochemical characteristics of apatite, sphene, and zircon from alkaline igneous rocks, Chinese Journal of Geochemistry, July – September 1989, Volume 8, Issue 3, pp 245-253

Long, K. R., Van Gosen, B. S., Foley, N. K., and Cordier, Daniel, 2010, The principal rare earth elements deposits of the United States – A summary of domestic deposists and a global perspective: U.S. Geological Survey Scientific Investigations Report 2010-5220, 96 p.

Love, J. D., 1960, Cenozoic Sedimentation and Crustal Movement in Wyoming, American Journal of Science, Bradley Volume, Vol. 258-A, pp. 204-214

Mariano, A. N. and Mariano, A. N. Jr., 2012, Rare Earth Mining and Exploration in North America, Elements, Vol. 8, pp. 369-376.

Mernejad, H., and Bell, K., 2006, Origin and Source Evolution of the Leucite Hills Lamproites: Evidence from Sr-Nd-Pb-O Isotopic Compositions, Journal of Petrology, Vol. 47, No. 4, pp. 2463-2489

Mitchel, R. H. and Bergman, S. C., 1991, Petrology of Lamproites, New York: Plenum

Nash, B. P., Perkins, M. E., Christensen, J. N., Lee, D, and Halliday, A. N., 2006, The Yellowstone hotspot in space and time: Nd and Hf isotopes in silicic magmas, Earth and Planetary Science Letters, Vol. 243, pp. 143-156

Obradovich, J.D., 1978, Age of volcanism at Togwotee Pass area in Wyoming: Geological Survey Research 1978, U.S. Geological Survey Professional Paper 1100, p. 183.

Obrebski, M., Allen, R. M., Pollitz, F., and Hung, S., 2011, Lithosphere-Asthenosphere Interaction beneath the Western United States from the Joint Inversion of Body-Wave Traveltimes and Surface-Wave Phase Velocities, Geophysical Journal International, vol. 185, pp. 1003-1021.

Pierce, K. L. and Morgan, L. A., Chapter 1: The track of the Yellowstone hot spot: Volcanism, faulting, and uplift, GSA Memoirs, Vol. 179, p. 1-54, doi: 10.1130/MEM179-p1

Prostka, H. J., Antweiler, J. C., and Bieniewski, C. L., 1972, Mineral Resources of the Du Noir Addition, Washakie Wilderness, Fremont County, United States Department of the Interior, Wyoming, Geological Survey Bulletin 1472

Putirka, K., 2008, Thermometers and Barometers for Volcanic Systems. In: Putirka, K., Tepley, F. (Eds.), Minerals, Inclusions and Volcanic Processes, Reviews in Mineralogy and Geochemistry, Mineralogical Soc. Am., v. 69, pp. 61-120.

Raymond, L.A., 2007, Petrology: The Study of Igneous, Sedimentary, and Metamorphic Rocks, Second Edition, p. 237

Rock, N. M. S., 1977 The nature and origin of lamprophyres: some definitions, distinctions, and derivations, Earth-Science Reviews, Vol. 13, Issue 2, p. 123-169, doi: 10.1016/0012-8252(77)90020-4

Sutherland, W. M., Gregory, R. W., Carnes, J. D., Worman, B. N., 2013, Rare Earth Elements in Wyoming, Wyoming State Geological Survey, Report of Investigation No. 65

Streckeisen, A., 1979, Classification and nomenclature of volcanic rocks, lamprophyres, cabonatites, and melilitic rocks: Recommendations and suggestions of the IUGS Subcommission on the Systematics of Igneous Rocks, Geology, Vol. 1, p. 331-335

Tse, Pui-Kwan, 2011, China's Rare-Earth Industry, USGS, Open-File Report 2011-1042

Verplanck, P. L., and Van Gosen, B. S., 2011, Carbonatite and alkaline intrusion-related rare earth element deposits - A deposit model: U.S. Geological Survey Open-File Report 2011-1256, 6 p.

Woolley, A. R. and Church, A. A., 2005, Extrusive carbonatites: A brief overview, Lithos, Vol. 85, p. 1-14

Woolley, A. R., Bergman, S. C., Edgar, A. D., Le Bas, M. J., Mitchell, R. H., Rock, N., Smith, B., 1996, Classifications of lamprophyres, lamproites, kimberlites, and the kalsilitic, melilitic, and leucite rocks, The Canadian Mineralogist, Vol 34., pp 175-186

Zhi li, L., and Yang, X., 2014, China's rare earth ore deposits and beneficiation techniques, 1st European Rare Earth Resources Conference (ERES 2014)

Appendix A - Sample Locations and Descriptions

Samples are listed in the order of collection. Northing and Easting coordinates correspond to UTM Zone 12T, NAD 27 CONUS. Sample ID's, locations, field descriptions, petrographic descriptions, and point counting analysis are listed for all samples relevant to Pilot Knob and Wildcat Hill field locations. Point counts averaged 758 counts per thin section sample.

Sample ID: ZD14-2

Northing: 4840360 **Easting:** 0576856

Description: Coarse to medium grained intrusive material that appears homogenous throughout outcrop. 50 m west of sample location, vesicles noted indicative of shallow instrusive bodies. Biotite (0.1 – 1mm), clinopyroxene (up to 3mm), and orthopyroxene crystals (up to 3 mm) with primarily plagioclase groundmass (~60%). In thin section exhibits hollocrystalline texture with crystalline groundmass. Groundmass is fine-grained euhedral to subeuhedral plagioclase feldspar (0.1 – 0.5mm). Weathered biotite exhibits basal cleavage. Poikilitic pyroxene shows twinning with intergrown subhedral 0.5 – 1.5mm plagioclase crystals.

Mode: Plagioclase groundmass (62.2%), clinopyroxene (15.9%), orthopyroxene (8.7%), biotite (6.7%), apatite (6.4%)

Sample ID: ZD14-5

Northing: 4840360 **Easting:** 0576856

Description: Course to medium grained intrusive material that appears to be a slight variation of sample ZD14-2. 30 m east of sample location, glacially deposited sandstone noted. 1-3mm clinopyroxene crystals throughout. In thin section, aphanitic, porphyritic groundmass with euhedral 0.1 – 0.5mm plagioclase crystals and weathered altered biotite Approximately 1 mm subhedral basal biotite crystals, zoned and fractured clinopyroxene, and altered 1 – 3mm orthopyroxene crystals.

Mode: Plagioclase groundmass (70.8%), clinopyroxene (14.4%), biotite (5.5%), orthopyroxene (4.5%), apatite (5.2%)

Sample ID: ZD14-6

Northing: 4840184 **Easting:** 0576555

Description: Homogenous with other Pilot Knob samples. Hand sample shows weathering rinds and slightly altered matrix. Thin section shows inequigranular, aphanitic, altered < 0.5mm plagioclase groundmass with incorporated highly altered biotite. Less weathered, <1 mm, altered, anhedral biotite throughout. Subhedral, zoned 1-3 mm clinopyroxene and orthopyroxene weathered with alteration rings. < 0.25 mm Garnet crystals also observed in thin section.

Mode: Plagioclase groundmass (63.6%), clinopyroxene (15.1%), biotite (8.1%), apatite (7.2%), orthopyroxene (5.6%)

Sample ID: MB13-2

Northing: 4840086 **Easting:** 0576911

Description: Appears homogenous with other Pilot Knob samples. Coarse to medium grained intrusive material. Biotite, clinopyroxene, and orthopyroxene phenocrysts with primarily plagioclase groundmass. Some alteration noted on phenocrysts. In thin section, sample appears identical to ZD14-5. Aphanitic, porphyritic feldspar groundmass with euhedral plagioclase crystals and highly weathered biotite. Zoned and weathered subhedral 1 - 3mm ortho/clinopyroxenes. <0.5mm vesicles noted throughout.

Mode: Plagioclase groundmass (71.7%), clinopyroxene (12.6%), biotite (5.8%), orthopyroxene (4.9%), apatite (4.9%)

Sample ID: ZD14-19a

Northing: 4851015 **Easting:** 0571657

Description: Vesiculated, platy hand sample with plagioclase, ortho/clinopyroxone, and primarily feldspar dominated groundmass. In outcrop, appears to be the "outer" portion of the intrusion. Lighter color indicative of slower cooling than ZD14-19b. In thin section, holocrystalline, fine, but inequigranular groundmass primarily composed of plagioclase and weathered biotite (< 0.2 mm crystals). Anhedral < 2mm orthopyroxene crystals with strongly weathered subhedral clinopyroxene exhibiting strong twinning.

Mode: Groundmass (73.2%), clinopyroxene (9.1%), plagioclase (8.5%) biotite (6.5%), orthopyroxene (2.7%)

Sample ID: ZD14-19b

Northing: 4851015 **Easting:** 0571657

Description: Blocky and glassy fine-grained sample. Outcrop shows vesicles and columnar jointing indicative of a shallow, fast cooling intrusive body. In thin section, holocrystalline, aphanitic groundmass consisting of plagioclase and biotite that has been nearly weathered to clay. Small vesicles (< 0.5mm) throughout. 1-3mm sub-anhedral ortho/clinopyroxene with significant weathering rinds and alteration. Trace garnets also noted in thin section.

Mode: Matrix (71.6%), plagioclase (8.5%), biotite (8.5%), clinopyroxene (7.6%), orthopyroxene (3.8%)

Appendix B - Electron Microprobe Data

All data collected for the polished thin sections samples used with the JEOL JXA-8600 electron microprobe is presented below. Every point analyzed was recorded on the basis of X and Y coordinates and annotated on a corresponding secondary electron image. Point labels correspond to the raw data label names. All SEM images are backscatter electron images showing representative crystals analyzed by the electron microprobe.

Biotite mineral recalculation found OH and H_2O amounts not recorded by the electron microprobe and was based on a 12 oxygen basis. Total oxygen moles for each molecule detected was calculated and summed. The conversion factor was then calculated by dividing 12 oxygens by the total oxygen moles preset. OH was then calculated by accounting for F and Cl moles then multiplying by the conversion factor. H_2O was then calculated, providing an accurate 'total' amount for the analysis.

$$Conversion\ Factor\ (C.F.) = \frac{12}{\Sigma\left(\frac{Amount\ of\ oxide}{Mol.\ Wt.\ oxide}\right)}$$

$$OH = 2 - \left[\left(\frac{Amount\ of\ F}{Mol.Wt.} * C.F.\right) + \left(\frac{Amount\ of\ Cl}{Mol.Wt.} * C.F.\right)\right]$$

$$H_2O = \left(\frac{OH * 9.0076}{C.F.}\right)$$

Feldspar recalculation followed similar steps as well, but found % values between An, Ab, and Or. The amount of Ca, Na, and K atoms for each sample was calculated, allowing each end member percent to be found. This process can be written as follows.

$$Amt.of\ Ca\ atoms = \left[\frac{\left(\frac{CaO\ in\ sample}{Mol.Wt.CaO}\right)}{\Sigma\left(\frac{Amount\ of\ oxide}{Mol.Wt.oxie}\right)}\right]$$

The amount of Na and K atoms can be found by substituting N_2O and K_2O in the previous equation respectively. After calculating the number of Ca, Na, and K atoms, the percent of each

end member can then be found (Na and K can be substituted for Ca to find Albite and Orthoclase end member amounts:

$$\%\ An = \left(\frac{Ca\ Atoms}{Ca\ atoms + Na\ atoms + K\ atoms}\right) * 100$$

Pyroxene recalculations focused on finding Fe_2, Mg, and Ca atoms in each sample in order to calculate the percentage of Wollastinite, Enstatite, and Ferrosilite. All calculations were performed in Excel:

$$\#\ Mg\ atoms = 4\left(\frac{Mole\ cations\ of\ Mg}{Total\ mole\ cations\ in\ sample}\right)$$

$$\%\ Enstatite = \left(\frac{\#\ of\ Mg\ atoms}{\#\ Mg\ atoms + \#\ Fe\quad atoms + \#\ Ca\ atoms}\right) * 100$$

After all mineral recalculations were completed, spreadsheets (Appendix C) were created showing percentage of different end members. IgPet software was then used to create ternary diagrams displaying these results.

Table 5-1 Biotite Electron Microprobe Data

Label	SiO2	TiO2	Al2O3	FeO	MnO	MgO	CaO	Na2O	K2O	F	Cl	OH	H2O	Total
bt1-1	37.15	3.67	15.14	8.9	0.0684	19.19	0.0369	0.6728	9.18	1.6593	0.0153	1.5801	2.9461	98.62
Bt3-2	37.63	3.68	15.51	8	0.0221	19.56	0.0224	0.5915	9.1	0.8629	0.0102	1.7838	3.3535	98.34
Bt7-1	48.97	0.6123	3.65	8.15	0.2249	14.92	19.93	0.3024	0.0128	0	0.0016	2.0002	3.8950	100.6
Bt7-4	49.12	0.5084	3.13	8.22	0.268	15	19.74	0.2987	0.0092	0.0641	0.0136	1.9861	3.8485	100.2
Bt8-1	36.42	4.29	15.51	9.08	0.1018	18.55	0.012	0.627	8.84	1.8919	0.0296	1.5199	2.8160	98.16
Bt9-1	36.54	3.9	15.26	9.27	0.0688	18.5	0.0346	0.6317	8.92	2.5166	0.0293	1.3572	2.5035	98.17
Bt9-2	37.01	3.34	15.67	8.84	0.0771	18.92	0	0.653	9	1.9546	0.0192	1.5040	2.7956	98.27
Bt9-3	36.86	3.38	15.78	8.62	0.1171	19.06	0.0042	0.5913	8.95	2.0327	0.0644	1.4901	2.7682	98.22
Bt9-4	37.37	3.6	15.39	9.24	0.0523	19.08	0.0226	0.6769	8.99	2.5625	0.0609	1.3599	2.5482	99.59

Table 5-2 Feldspar Electron Microprobe Data

Label	SiO2	Al2O3	FeO	MgO	MnO	CaO	Na2O	K2O	Total	An	Ab	Or
ZD14-5 Fsp1-1	50.46	31.34	0.8812	0.1113	0	13.09	3.32	0.4991	99.7	49.3755	46.0676	4.5568
Fsp4-1	50.89	30.21	0.9153	0.1347	0	12.64	3.52	0.6389	98.95	46.5815	47.7194	5.6990
ZD14-6 Fsp5-1	51.91	29.42	0.7299	0.0402	0.0195	11.09	4.44	0.4067	98.06	39.0390	57.4957	3.4653
ZD14-5 Fsp7-1	50.67	30.41	0.9074	0.1305	0	13.03	3.48	0.501	99.13	48.1802	47.3358	4.4840
Fsp7-2	51.1	30.3	0.9411	0.1246	0.0056	12.8	3.46	0.5443	99.28	47.6802	47.4122	4.9076
Fsp7-3	50.59	30.84	0.979	0.1084	0	12.97	3.46	0.4973	99.44	48.2125	47.3131	4.4744
Fsp7-4	46.1	33.89	0.6954	0.0759	0.0223	16.79	1.5889	0.1788	99.34	72.7856	25.3383	1.8761
Fsp7-5	51.25	30.25	0.8374	0.1366	0.0181	12.43	3.71	0.525	99.16	45.4505	49.9030	4.6465

Table 5-3 Pyroxene Electron Microprobe Data

Label	MgO	Na2O	Al2O3	SiO2	CaO	K2O	TiO2	FeO	MnO	Cr2O3	Total	Wo	En	Fs
ZD14-5 Px1-2	16.92	0.2073	2.4007	52.19	22.22	0	0.4035	4.69	0.103	0.2004	99.33	44.9587	47.6344	7.4070
ZD14-5 Px1-3	16.02	0.2686	3.74	50.16	22.08	0.0191	0.621	5.56	0.0959	0.3298	98.9	45.3295	45.7610	8.9095
ZD14-5 Px2-1	16.14	0.2387	2.9021	51.29	21.86	0.0028	0.4742	5.92	0.1202	0.1031	99.04	44.6688	45.8890	9.4422
ZD14-5 Px2-3	15.39	0.2497	4	49.87	22.02	0.0065	0.5874	5.41	0.1224	0.3647	98.03	46.2058	44.9333	8.8608
ZD14-5 Px1-1	15.37	0.2658	4.5	48.89	22.09	0	0.7317	6.12	0.0989	0.369	98.43	45.7798	44.3203	9.8998
Px1-2	15.32	0.2687	3.73	50.15	21.84	0.013	0.5975	6.68	0.1838	0.0018	98.78	45.1517	44.0688	10.7794
Px2-1	17.23	0.1987	2.1731	51.88	21.66	0.0041	0.3885	4.96	0.0823	0.1888	98.77	43.7529	48.4267	7.8204
Px2-3	17.19	0.2164	2.129	51	21.85	0.0099	0.4343	5.09	0.145	0.1365	98.2	43.9275	48.0852	7.9873
Px2-4	15.27	0.237	3.7	50.03	21.58	0.0065	0.6549	6.55	0.1363	0.0805	98.24	45.0154	44.3199	10.6647
Px2-5	16.08	0.2208	2.7291	51.33	21.64	0.0045	0.4756	5.52	0.1143	0.1202	98.24	44.7827	46.3009	8.9164
Px2-6	0.0974	2.1047	33.24	45.96	15.72	0.2245	0.0135	0.6724	0	0.0235	98.06	95.9686	0.8273	3.2041
Px3-1	15.9	0.2855	2.6179	51.92	21.28	0.009	0.4299	6.41	0.1992	0.0179	99.06	43.9610	45.7030	10.3360
Px4-1	15.86	0.2436	3.76	50.32	22.28	0.0047	0.585	5.25	0.0739	0.2533	98.63	45.9899	45.5514	8.4587
Px5-1	17.03	0.2445	2.3491	48.09	21.9	0	0.4109	5.12	0.0823	0.0988	95.33	44.1605	47.7810	8.0586
Px5-2	15.09	0.247	4.48	49.28	21.84	0	0.7874	7.15	0.1154	0.0821	99.09	45.1081	43.3652	11.5267
Px5-3	16.22	0.256	2.9296	45.92	22.32	0.0054	0.4379	5.01	0.1547	0.3879	93.64	45.7387	46.2478	8.0136
ZD14-6 Px6-1	16.49	0.243	2.8181	52.07	22.07	0.0117	0.4449	4.75	0.0809	0.5613	99.54	45.2981	47.0922	7.6097
Px6-3	16.24	0.2492	3.01	51.43	21.86	0.0032	0.4938	5.51	0.1394	0.1669	99.1	44.8345	46.3446	8.8209
Px7-1	16.72	0.236	2.4584	52.25	21.79	0.0128	0.3862	5.15	0.1269	0.1168	99.24	44.4024	47.4063	8.1913
Px7-2	15.67	0.2559	3.64	50.86	22.06	0.0072	0.603	5.48	0.0711	0.2027	98.85	45.8241	45.2907	8.8852
Px8-2	17.21	0.1753	1.6689	52.69	21.1	0	0.3466	5.13	0.127	0.0126	98.47	43.0172	48.8193	8.1635
Px8-3	16.07	0.2494	3.39	51.57	21.92	0.0097	0.4903	5.24	0.1255	0.07	99.13	45.3175	46.2267	8.4558
Px9-1	16.57	0.2402	2.6368	52.16	21.87	0	0.3618	4.9	0.1297	0.3415	99.21	44.8614	47.2931	7.8455
Px9-2	17	0.1694	1.9765	52.68	21.81	0.0029	0.326	5.18	0.1171	0.0305	99.28	44.0544	47.7786	8.1670
Px10-2	16.63	0.3038	3.67	51.2	21.4	0.0034	0.5144	5.29	0.1324	0.1598	99.31	43.9714	47.5444	8.4842
Px10-3	16.91	0.228	2.2454	52.64	21.93	0.0029	0.3365	4.59	0.1367	0.1583	99.18	44.7175	47.9770	7.3055
Px10-4	14.69	0.2995	4.16	49.97	20.64	0.0128	0.6967	7.87	0.2277	0.0196	98.59	43.7080	43.2836	13.0084
Px11-1	0.1049	3.47	31.06	50.42	13.6	0.1499	0.0113	0.6083	0	0	99.42	95.6348	1.0264	3.3388
Px13-1	0.0019	6.02	27.87	56.3	8.98	0.379	0.0233	0.146	0.0084	0	99.72	98.7182	0.0291	1.2528

Figure C 5-1 Electronic scan of ZD14-5 thin section indicating analyzed crystal locations.

Figure C 5-2 Electronic scan of ZD14-6 thin section indication analyzed crystal locations.

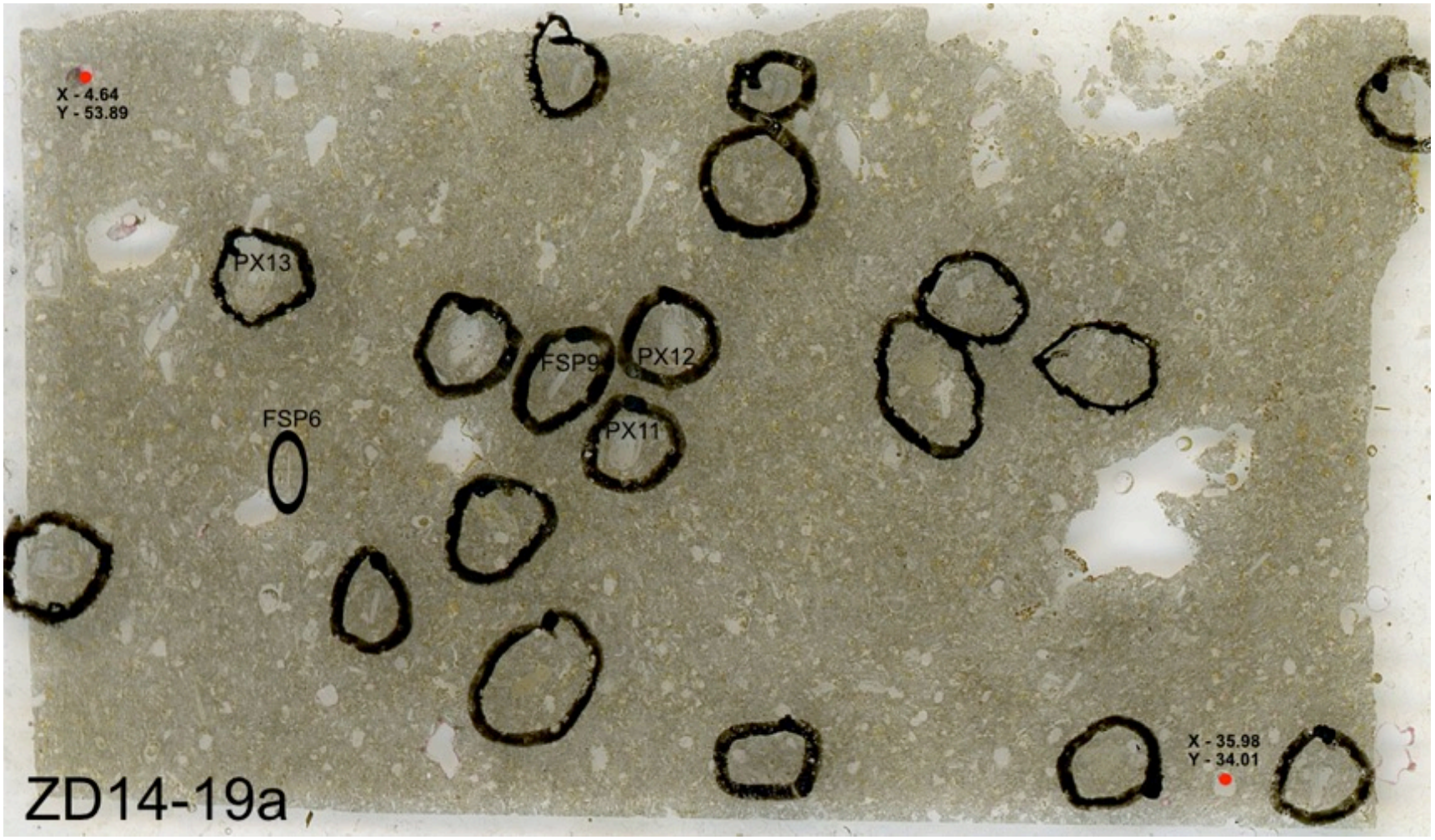

Figure C 5-3 Electronic scan of ZD14-19a indicating analyzed crystal locations.

Biotite 1

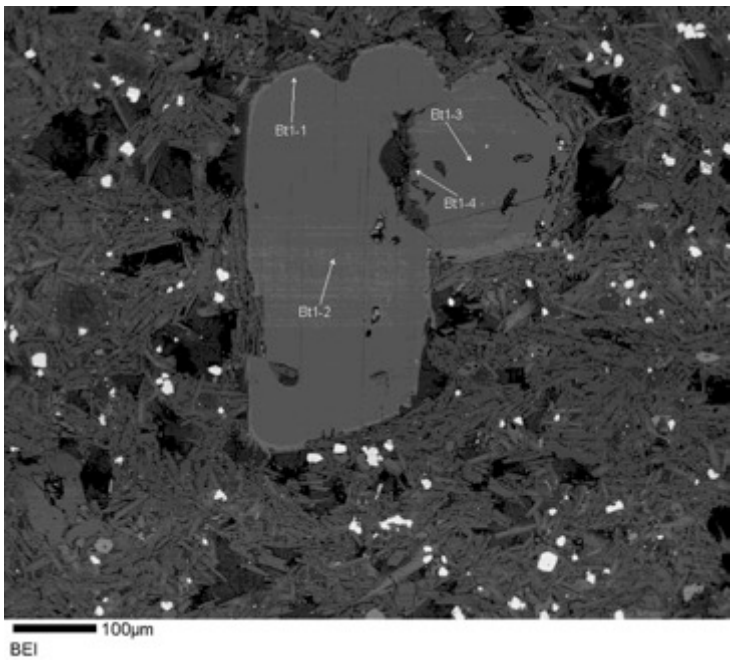

Biotite 2

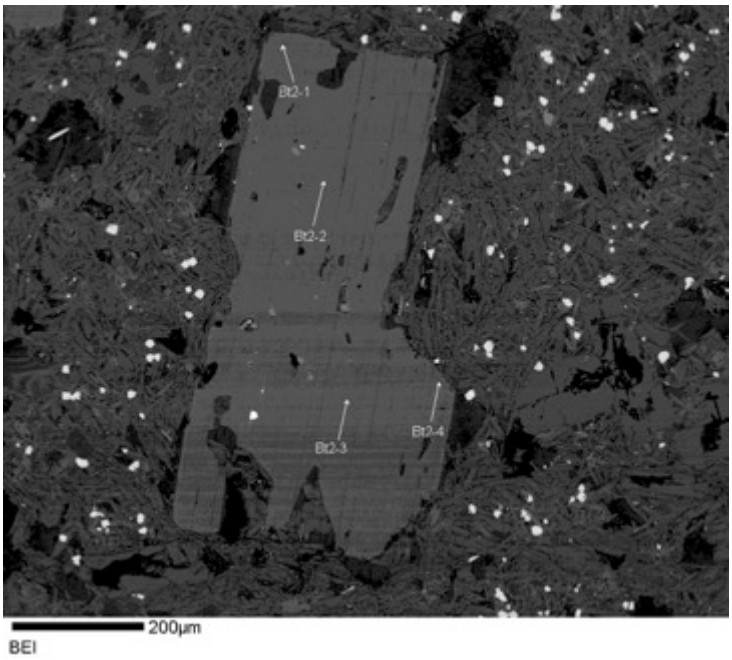

Biotite 7

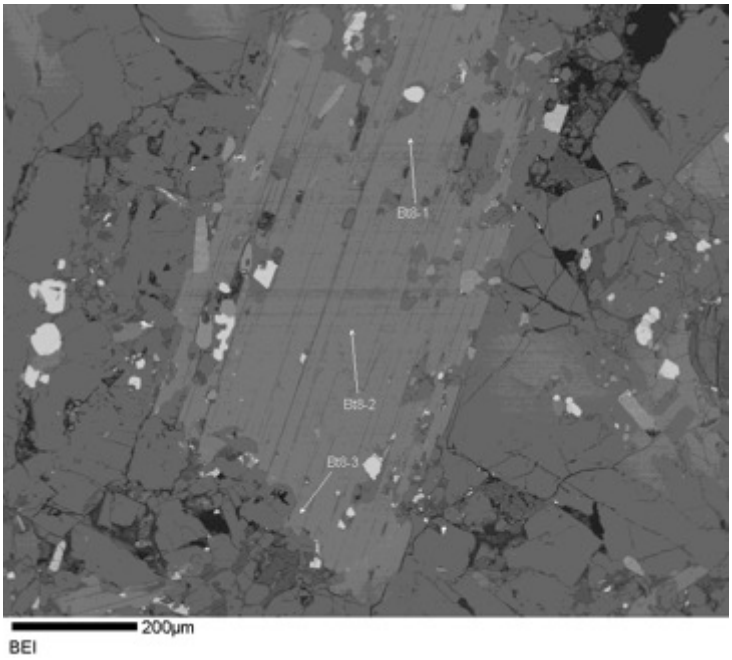

Feldspar 1

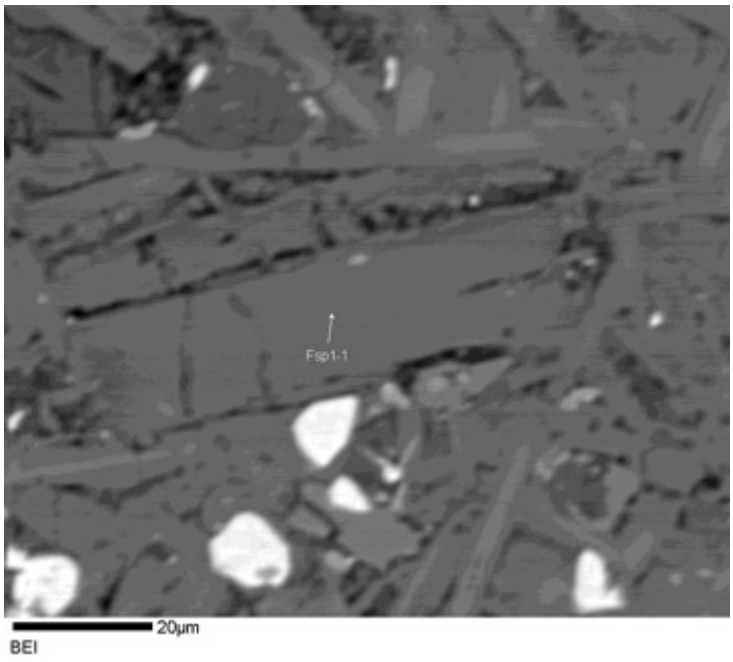

Feldspar 2

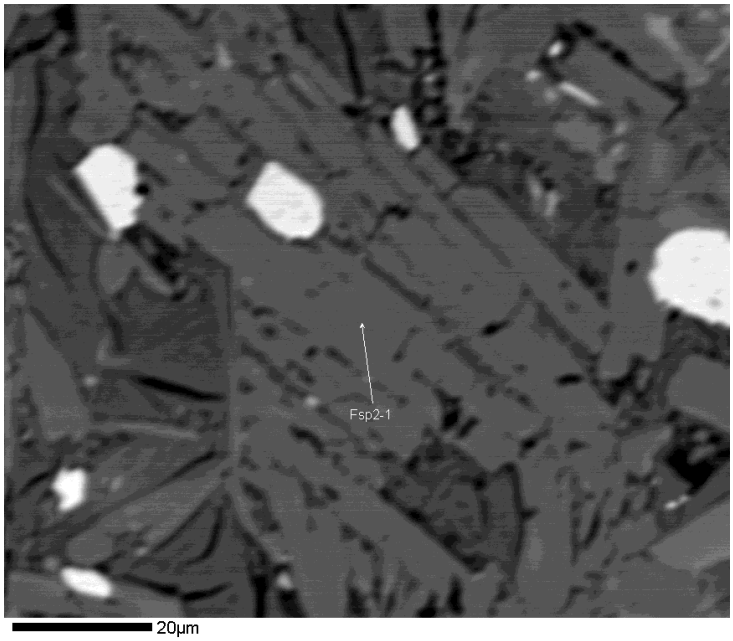

Feldspar 7 and Elemental Maps

Backscatter electron images using EDS from CU EMPA to differentiate between Ca and Na. Images show the zoning pattern on the inside of the crystal. Inner portion is more Na-rich and outer ring is Ca-rich feldspar. Horizontal lines at top and near bottom of images are scanning electron microscope imaging artifacts.

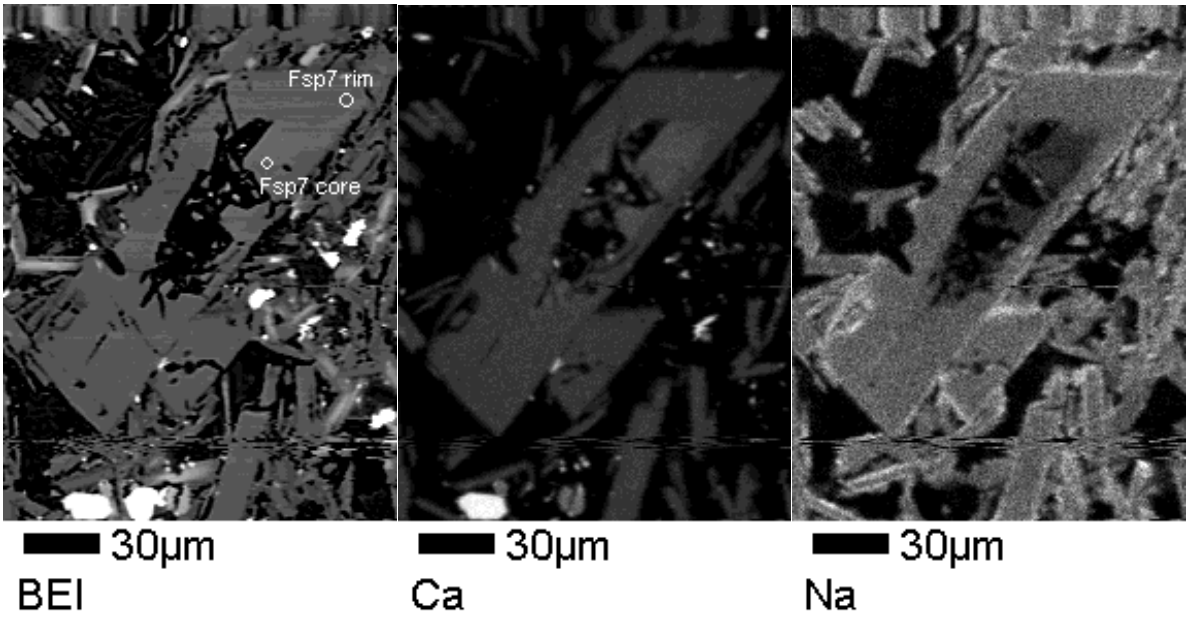
Fsp7 rim
Fsp7 core
30µm
BEI
30µm
Ca
30µm
Na

Pyroxene 1

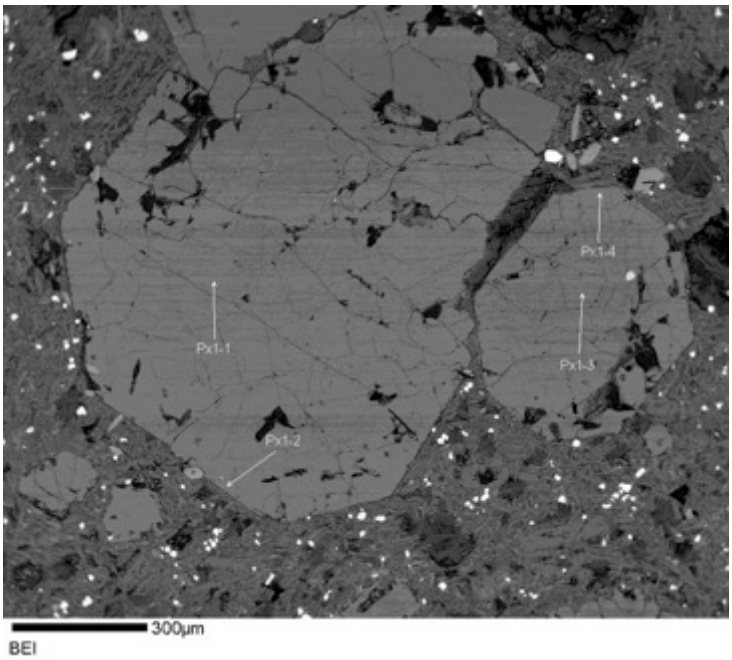
Px1-1
Px1-2
Px1-3
Px1-4
300µm
BEI

Pyroxene 2

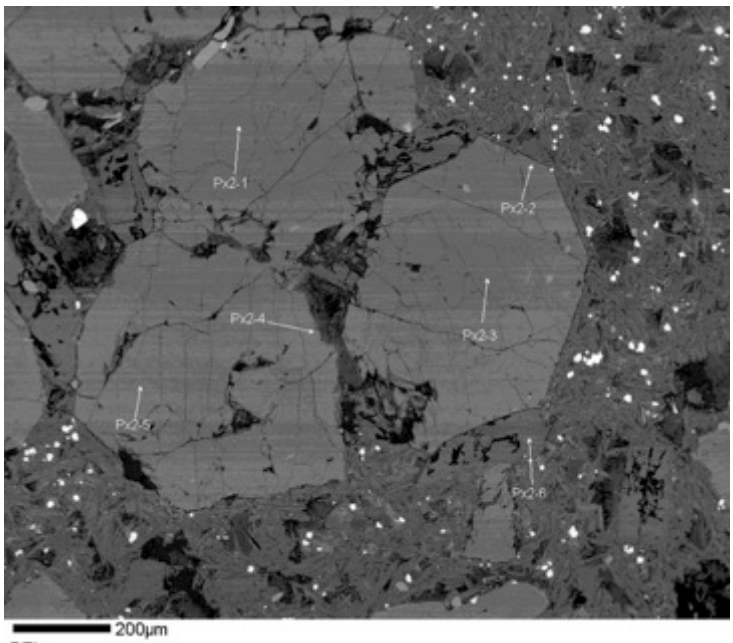

Pyroxene 3

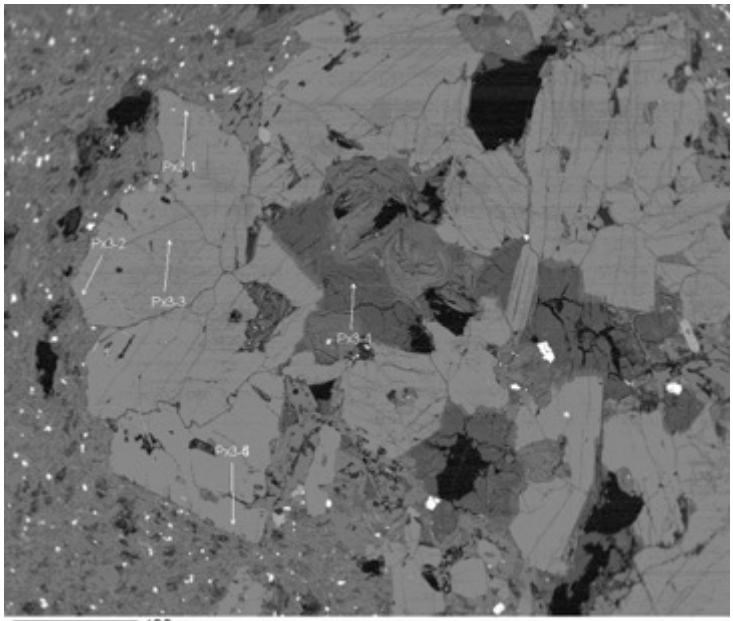

Pyroxene 13